2A.1. Introduction

To date, many efforts have been made in the fabrication of nanostructured materials having different morphologies such as spheres, wires, ribbons, belt, tube, sheets etc. Each such shape and morphology imparts unique physical properties to the material. Even, different morphologies of the same material play an important role during their applications. For example, Lu et al synthesized Ga doped ZnS nanostructures having intercrossed sheet like morphology (nano-wall) which, they claimed, are promising candidate materials for photocatalysts and applicable as photodetectors, optical switches, and sensors in the visible light region due to high surface area of nano sheets [1]. Li et al described the one-pot synthesis of ZnS nanospheres and showed that the same were exhibited high performance in prohibiting the growth of *E.coli* bacteria [2]. Lu, F et al proposed that the ZnS nanobelt array may be the promising candidate for various field emission applications such as flat-panel displays and vacuum microelectronic devices [3].

The transition metal ions such as Mn^{2+},Fe^{2+},Co^{2+},Ni^{2+} etc when introduced as dopant, modify the optical, chemical and magnetic properties of the material. For example, Dong et al. synthesized Mn^{2+}, Co^{2+} and Ni^{2+} doped clew-like ZnS nanostructures by hydrothermal route [4]. Bang et al. prepared Ni^{2+}doped ZnS hollow microspheres by ultrasonic spray pyrolysis as efficient photocatalyst [5]. Arai et al. reported Cu^{2+} doped ZnS hollow nanoparticles as efficient photocatalyst in comparision to the copper-free ZnS- hollow nanoparticles to generate H_2 through photocatalytic decomposition of HS^- ion in Na_2S solution [6]. Kar et al. reported white light emission from Mn^{2+} doped ZnS nanorods by a solvothermal approach [7].

These applications are due to their stability and durability at high temperatures, inertness and non-toxicity [8]. The band gap energy is one of the factors which decide the optical properties and subsequent applications [9]. When electrons in the valence band are excited to the conduction band they leave holes behind in their original band. If such transition is taking place with conservation of momentum, then the

material called as direct band gap emitters. If it is not, then such transitions are forbidden and the band gap should be tuned by introducing impurity ions (doping) in a semiconductor host. This provides extra energy levels between valence band and conductance band and facilitates the energy transfer processes between electron-hole pairs faster than the non-radiative recombination process [10]. This results in enhancement of optical properties. Another way of tuning band gap is to convert bulk semiconductors to nanoscale material. At nanoscale the energy levels at the top of the valence band and bottom of the conduction band becomes discrete. Therefore, not only the optical properties are modified but also new properties are generated because of quantum confinement of electron-hole pairs at the crystallite boundaries [11, 12]. These nanocrystallites magnetically couple with each other and induce magnetic properties in the material.

Both strategies mentioned above can be exploited during synthesis of colloidal nano particles in solution using suitable dopant ions particularly from the transition metal series (from d or f – block elements). Recently, X.Peng propounded strategies on Band Gap and Composition Engineering on a Nanocrystal (BCEN) in solution. Peng has compared the idea of inducing multiple functionalities in a single nanostructure such as enzyme performing two sequential reactions [13].

In this study, we report a simple wet chemical method to dope Ni^{+2} ions in ZnS nanoparticles in different phases. We observed the change in morphology of ZnS nano particles with dopant (Ni^{+2} ion) concentration. The optical and magnetic properties of the synthesized material are evaluated systematically with dopant (Ni^{+2}) concentration. Thus, in summary, it is possible to induce multiple functionalities in single ZnS/M^{+n} nanoparticle and exploit the same by changing the external stimuli.

2A.2 Experimental

(a) Materials

Analytical Grade Zinc acetate $(CH_3COO)_2Zn.2H_2O$, Nickel acetate $(CH_3COO)_2Ni.4H_2O$, Sodium sulphide $Na_2S.xH_2O$, Sodium hydroxide NaOH and 2-Mercaptoethanol $HSCH_2CH_2OH$ were obtained from Loba Chemie Mumbai, India and used as received.

(b) Synthesis of ZnS nanoparticles

The methanolic solution of zinc acetate (0.025mol) and nickel acetate (3.456×10^{-4}mol; for 1.25%) were mixed under continuous stirring followed by addition of Mercaptoethanol (0.025mol). An aqueous solution of NaOH (1M) was added to maintain the pH (10.2) and sodium sulphide solution (0.025mol) was injected into the reaction mixture. The reaction mixture was continuously stirred for 3 h to get a homogenous stabilized dispersion. The resulting precipitate were separated by centrifugation at 8000 rpm, washed with deionised water several times and then dried at 100 °C to obtain a ZnS:Ni^{2+} powder sample. Other samples of ZnS nanoparticles with different dopant concentration were prepared by taking nickel acetate concentrations 6.952×10^{-3} mol (2.5%), 1.386×10^{-3}mol (5.0%) and 2.778×10^{-3}mol (10.0%) respectively (as shown in scheme 1). Similarly, blank (without dopant) ZnS nanoparticles were synthesized by the same method.

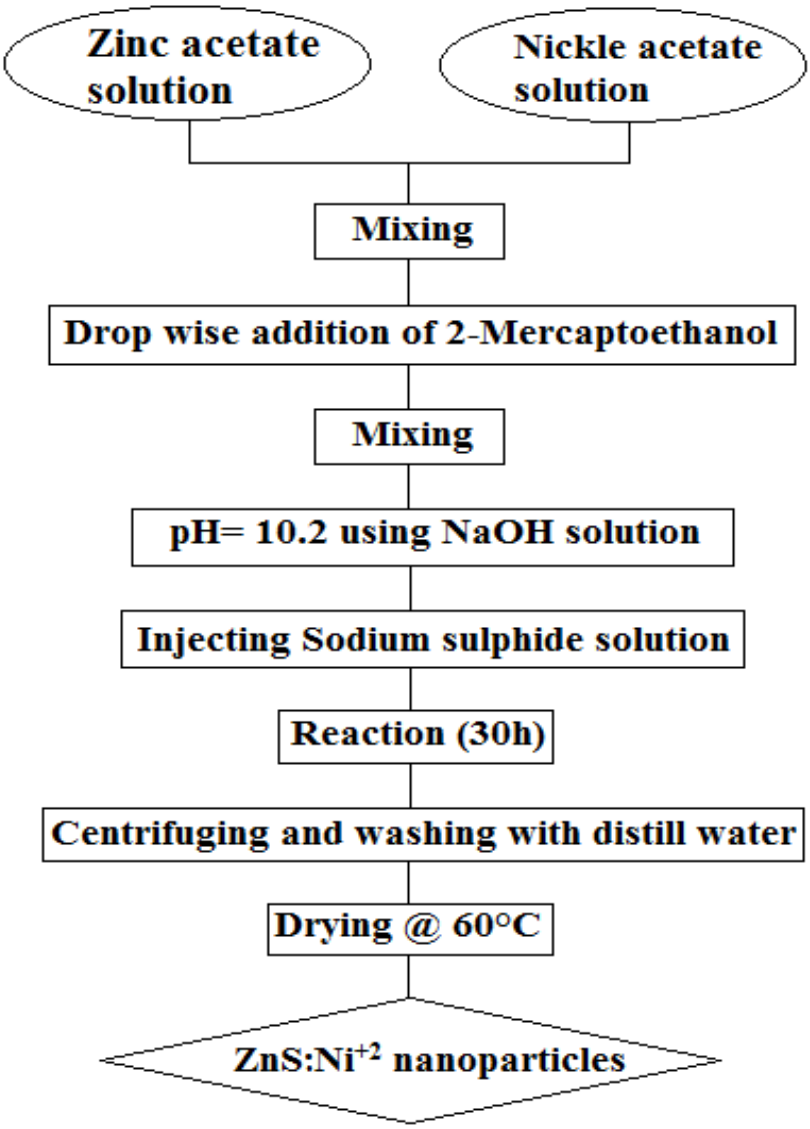

Scheme 1 Experimental procedure to synthesize ZnS:Ni^{2+} nanoparticles.

2A.3. Results and Discussion

2.A.3.1 X-ray diffraction (XRD)

The X-ray diffraction pattern of the prepared ZnS and ZnS:Ni^{2+} nanoparticles are shown in Figure 2A.1. The XRD peaks were broad as compared to bulk ZnS due to the nano regime. The XRD patterns of all the samples are having main diffraction features corresponding to (111), (220) and (311) planes. It has been observed that out

of these three main features, the peaks corresponding to (311) merged in background. The XRD patterns of undoped and doped with 1.2 and 2.5% Ni^{+2} are well matched with the standard cubic ZnS (JCPDS card No. 79-0043). However, a shoulder of weak intensity corresponding to (101) planes appeared (*) at 5% concentration of Ni^{+2}. At 10% concentration of Ni^{+2}, the broad peak corresponded to (111) planes in cubic phase, became distorted and (101) shoulder became more intense along with the (002) and (100) peaks. This distortion of peaks clearly indicates that phase changes from cubic sphalerite to hexagonal wurtzite (JCPDS card No. 79-2204 for 10% Ni^{+2}). On the basis of the Full Width at Half-Maximum (FWHM) intensity of XRD peak and the Debeye-Scherrer formula [14],

$$D = k \lambda / \beta \cos\theta \quad \text{..... (1)}$$

the average crystallite size D was calculated, here, k (=0.9) is a geometric factor, λ (=0.154 nm) is the wavelength of X-rays, β, the FWHM of diffraction angle and θ, the diffraction angle. For the calculation of FWHM, the first two intense peaks corresponding to (111) and (220) planes were selected and the average crystallite size for Ni^{2+}doped ZnS and undoped ZnS samples were calculated which are in the range of 1-1.5 nm (Table. 2A.1). Very small particle size could be due to basic conditions maintained during the synthesis and also due to the presence of the capping agent, (mercaptoethanol). Both of these factors directly affect the steric and electrostatic repulsions who prevent further growth of the particles. From the XRD patterns it can also be concluded that Ni^{+2} ions occupy the lattice sites or interstitial space of cubic or hexagonal close packed ZnS host and did not form a separate phase as in NiS.

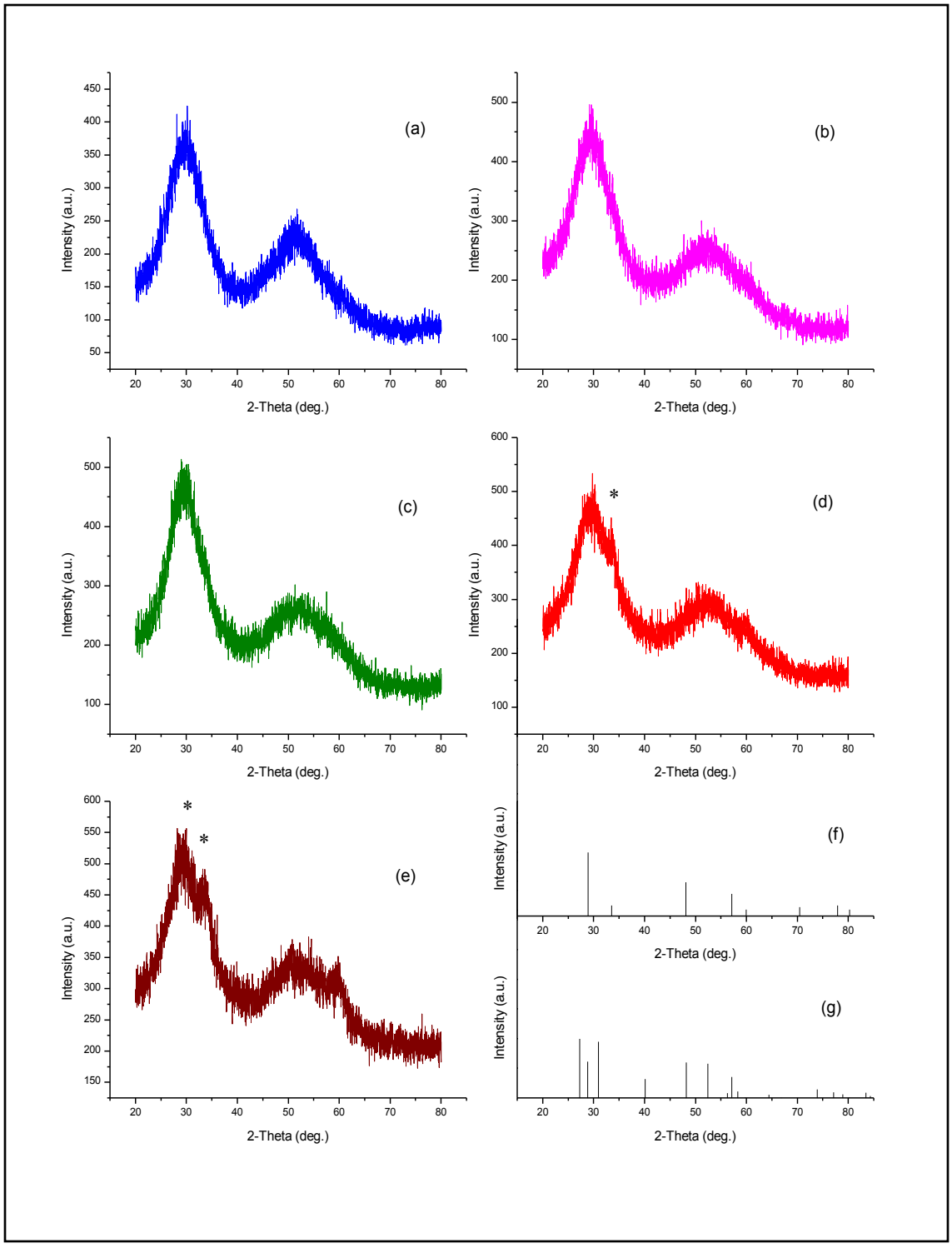

Figure 2A.1 XRD patterns of ZnS samples: (a) ZnS undoped (b) ZnS:Ni^{2+}(1.2%) (c) ZnS:Ni^{2+}(2.5%) (d) ZnS:Ni^{2+}(5.0%) (e) ZnS:Ni^{2+}(10.0%) (e) standard cubic ZnS bulk pattern as per (JCPDS card No. 79-0043) and (f) standard wurtzite ZnS bulk as per (JCPDS card No. 79-2204) .

Energy Dispersive X-ray analyses (EDX)

EDX spectra of the undoped ZnS and ZnS:Ni^{2+}(10.0%) samples are shown in Figure 2A.2(a) and 2A.2(b). The actual concentration of Ni^{+2} doped in the sample are given in Table 2A.2. Semi-log plot of the actual amount of Ni (in %w/w) present in the ZnS matrix against the original amount taken for doping to synthesize the material have been depicted in Figure 2A.2(c). It can be noted that the actual amount found in the matrix was dependent upon the original amount taken for doping. This behavior shows that sufficient lattice site defects or interstitial voids are available in the host matrix (ZnS NPs). The ionic radius of Ni^{2+} (72 pm) is smaller than that of Zn^{2+} (74 pm) which supports the higher diffusion probability of Ni in ZnS sites. It was observed (Table 2A.2) that in case of 10% dopant concentration, the actual amount present in the host is only 4%. We propose that as the concentration of the dopant ion in host matrix increases, the tendency of the host material to eject the same toward the surface or outside also increases. The oxygen detected in the sample could be contributed by residual NaOH present in the sample (as ZnS cannot be oxidized under basic conditions [15].

Dynamic light scattering (DLS)

DLS spectra (Figure 3A.2) demonstrate that the particle size ranging from 300- 850 nm (Table 2A.3). This might be due to rapid aggregation of NPs by Brownian motion because of smaller size and larger diffusion coefficient. The intensity of scattered light detected in DLS becomes greatly magnified if aggregate of micron size particles are present in the solution.

Inductive coupled plasma atomic emission spectroscopy (ICP-AES)

The amount of Ni^{+2} in the doped ZnS NPs was also determined by ICP-AES (Table 2A.2). It can be seen that the Ni/Zn ratio used for the synthesis (at %) and the same calculated from ICP-AES analysis are comparable. The interesting feature of the

results is that at 5% concentration, the Ni/Zn ratio is higher than that of predicted but at the same time it can be seen that the amount of Zn in the sample decreases and of Ni increases. This observation reveals that the Ni atoms replace the Zn atoms from the sites more than occupying the interstitial sites (of ZnS crystal lattice).

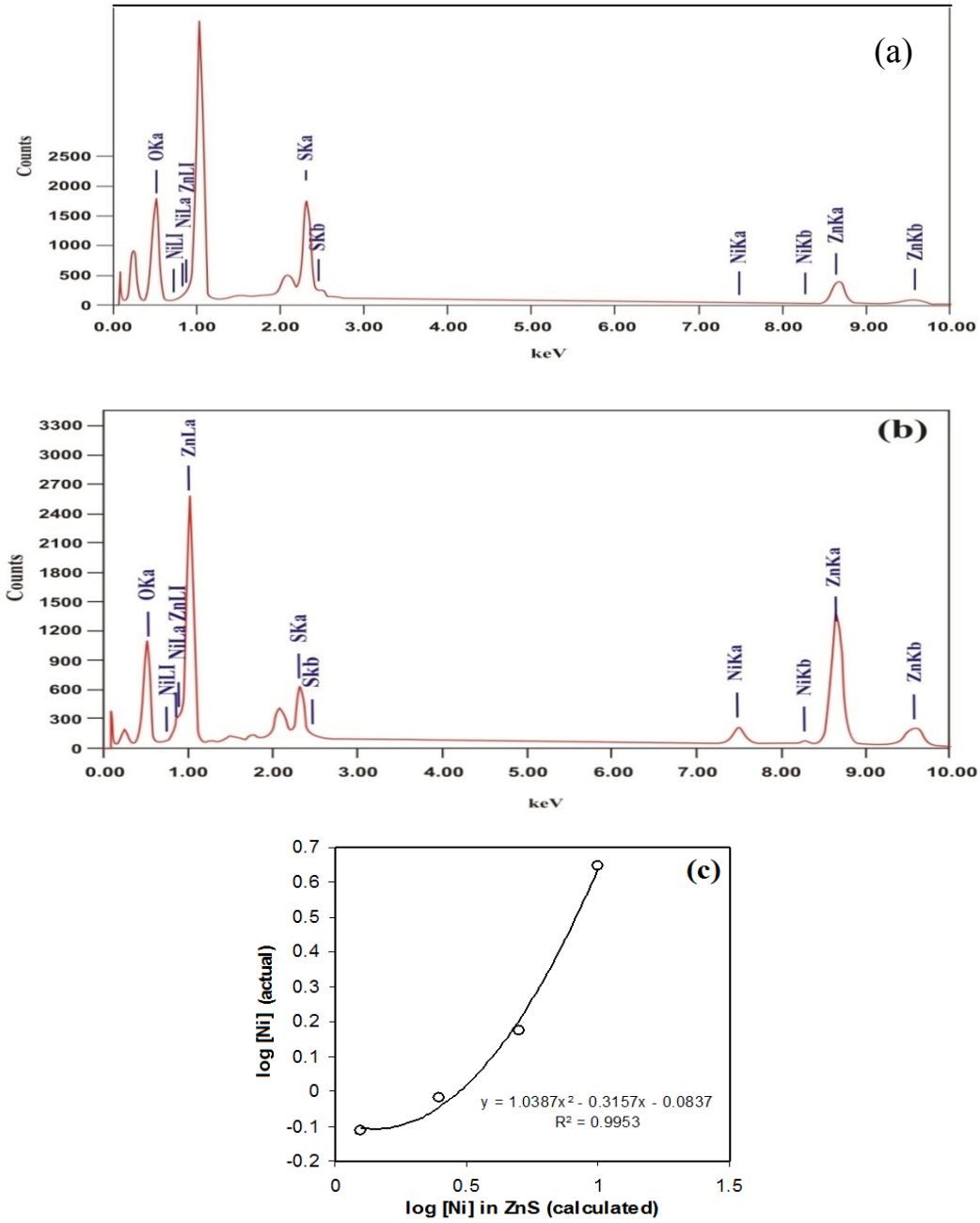

Figure 2A.2 EDX analysis of ZnS nanoparticles capped with mercaptoethanol (a) undoped ZnS and (b) ZnS:Ni^{+2} (10%) (c) Semilog plot indicating concentration of Ni in nano ZnS host.

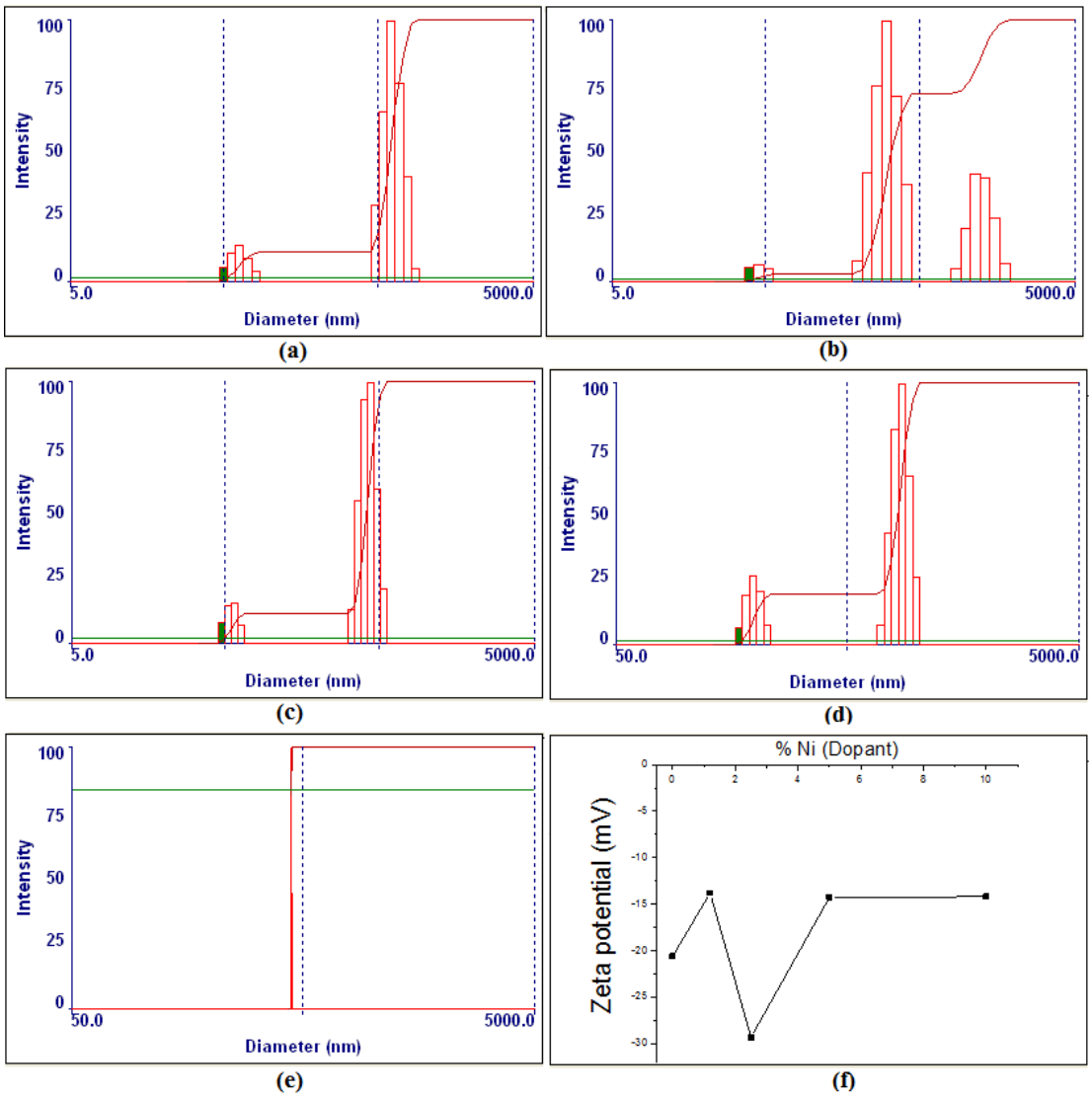

Figure 3A.3 Hydrodynamic diameter of ZnS nanoparticles (a) ZnS undoped (b) ZnS:Ni^{2+}(1.2%) (c) ZnS:Ni^{2+}(2.5%) (d) ZnS:Ni^{2+}(5.0%) (e) ZnS:Ni^{2+}(10.0%) and (f) Zeta potential of ZnS nanoparticles with different % Ni ion concentration .

Fourier Transform Infrared Spectroscopy (FT-IR)

The presence of 2-mercaptoethanol in 2-mercaptoethanol capped doped and undoped ZnS nanoparticles was confirmed by FTIR spectra as shown in Figure 2A.4. The obtained FTIR spectra of the as-synthesized nanoparticles were compared with FTIR spectra of bulk ZnS and neat 2-mercaptoethnol. Broad band around 2491 cm^{-1} can be

assigned to S—H stretching. A broad band about 3515 cm^{-1} can be assigned for O—H. The weak bands around 1457 cm^{-1} and 1537 cm^{-1} can be assigned to the symmetric and asymmetric stretching of COO^- respectively which may arise from acetate group of the precursor. A band around 878 cm^{-1} can be assigned to C—SH bending. The bands at 1166, 1339 can be assigned to CH_2 wagging and OH bending respectively. These observations reveal that capping of doped and undoped nanoparticles was due to adsorption of 2-mercaptoethanol.

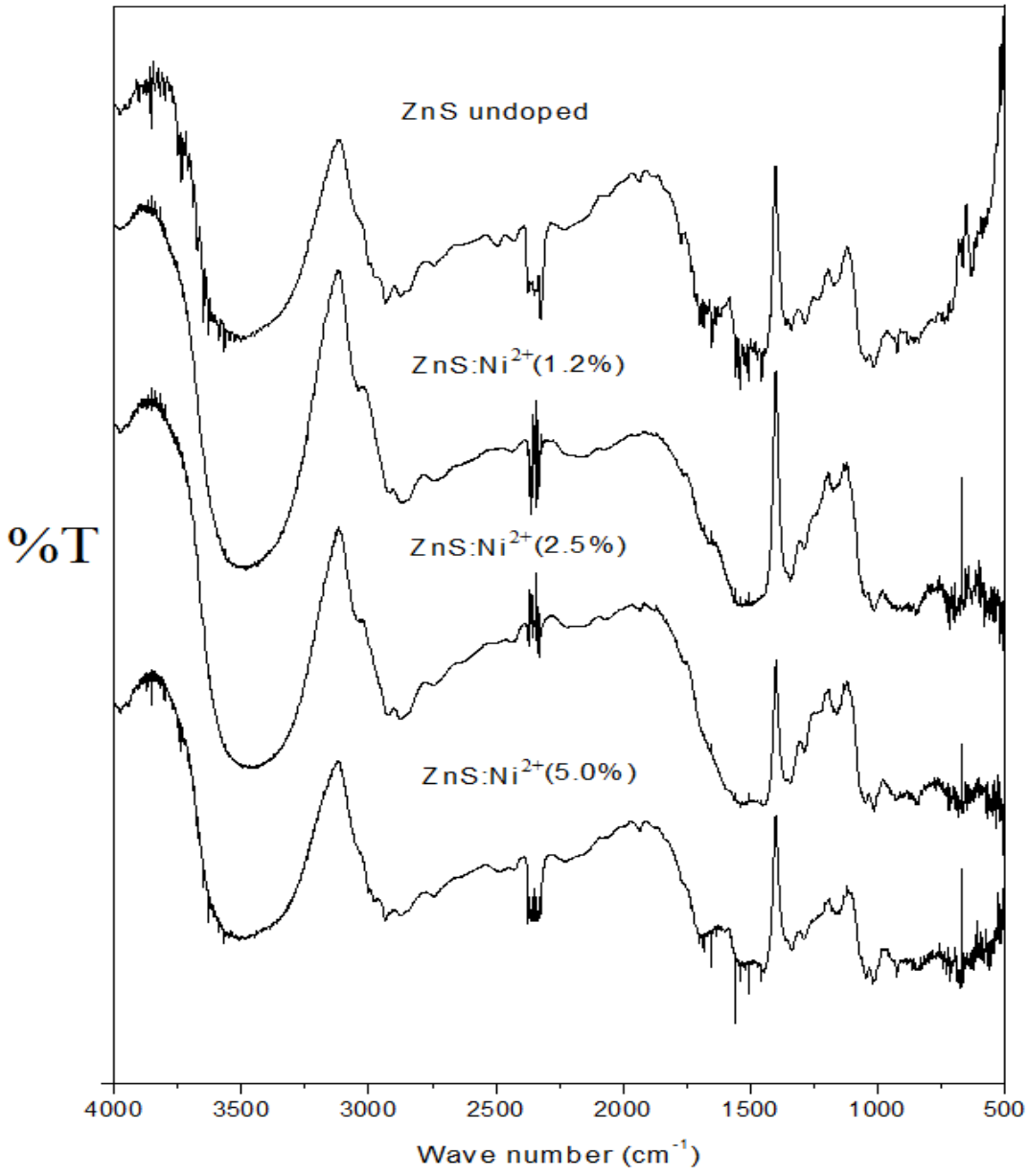

Figure 2A.4 FTIR specta of undoped and ZnS:Ni^{2+} nanoparticles.

Table 2A.1 Particle size of ZnS nanoparticles calculated from Effective mass model and Debeye-Scherrer formula.

Sample	Absorption edge (nm)	Band gap (eV)	Particle size from UV (nm)	Particle Size from XRD (nm)
Bulk ZnS	337	3.68	-	-
ZnS NP undoped	280	4.43	1.7	1.0
ZnS: Ni^{2+} (1.2%)	285	4.35	1.8	1.1
ZnS: Ni^{2+} (2.5%)	286	4.34	1.8	1.1
ZnS: Ni^{2+} (5.0%)	290	4.28	1.9	1.0
ZnS: Ni^{2+} (10.0%)	290	4.29	1.8	1.0

Table 2A.2 Percentage Ni (atomic wt%) as dopant in ZnS host determined by EDX and ICP-AES techniques and quantum yield.

Amount of Ni doped (at.% used in synthesis)	Actual Amount of Ni in ZnS matrix (from EDX) (%)	Ni/Zn (at. %) determine by ICP	Ni (wt.%) determine by ICP	Zn (wt.%) determine by ICP	Quantum Yield (QY)
0	-	-	-	-	11.45
1.25	0.77	1.31	0.76	58.58	40.95
2.5	0.96	2.59	1.53	58.81	15.52
5.0	1.50	6.24	2.82	45.24	-
10	4.45	10.28	5.24	50.93	-

Table 2A.3. Hydrodynamic diameter by dynamic light scattering and zeta potential.

Sr.No.	Amount of Ni doped (calculated) (%)	Hydrodynamic diameter (nm)	Zeta potential (mV)
1	0	595	-28.84
2	1.25	299	-13.79
3	2.5	431	-29.29
4	5.0	855	-14.24
5	10	443	-14.19

Transmission Electron Microscopy (TEM)

The morphology of the nanoparticles is studied by TEM analysis (Figure 2A.5). The undoped ZnS NPs were spherical having diameter ~32 nm. The Selected Area Electron Diffraction (SAED) pattern of undoped ZnS nanoparticles (Figure.2A.5 inset) reveals the crystalline nature of the materials. The TEM image of Ni^{2+} (2.5%) doped ZnS NPs shows the formation of nanorods. The average size of a nanorod is ~95 nm length and ~30 nm breadth. The SAED pattern shown as inset indicates the material is crystalline.

Scanning Electron Microscopy (SEM)

The morphologies of all the samples were investigated with Scanning Electron Microscopy (SEM), as shown in figures (2A.6 a–d). ZnS nanoparticles without any dopant showed the spherical morphologies (figure 2A.6a). When 1.2% Ni^{2+} ions were introduced as dopant, ZnS dots with short armed multipods morphologies were obtained (figure 2A.6b). This type of morphology could be due to insufficient capping of the growing nuclei by ligands. At the time of nucleation if sufficient amount of capping ligands adsorbed on the growing nuclei then resulting shape would be dot which can be seen in the first case. But it could also be possible to let the

ligands adsorb on the surface of nuclei after some initial growth by tuning the reaction parameters. In our case this was achieved in presence of 1.2% Ni^{2+}. It was observed that due to presence of Ni^{2+} ions, the nuclear growth processes became extended resulting into sizable volume of crystal nuclei. These may be due to the competition among Ni^{2+} ions and marcaptoethanol molecules to interact with preferred surface planes of the material. Being smaller in size and charged, Ni^{2+} interacted more strongly than thiols resulted in anisotropic growth in the direction of planes where Ni^{2+} ions present in more numbers (Ni^{2+} can't hinder the growth of the material like thiols). Now, the surface planes which were grown enough and preferred by thiols, the single molecule of thiol was not capable to cover whole crystallite surface. Therefore, the crystal growth would be hindered from the sites where capping ligands were present; however, it persisted from the sites where ligands were absent. This causes different pods like morphologies (Figure 2A.7). When concentration of dopant ions was increased to 5.0%, the changes in morphologies of the ZnS crystals were occurred. The nano sheets with curved surfaces and almost separated from each other were observed (Figure 2A.6c).

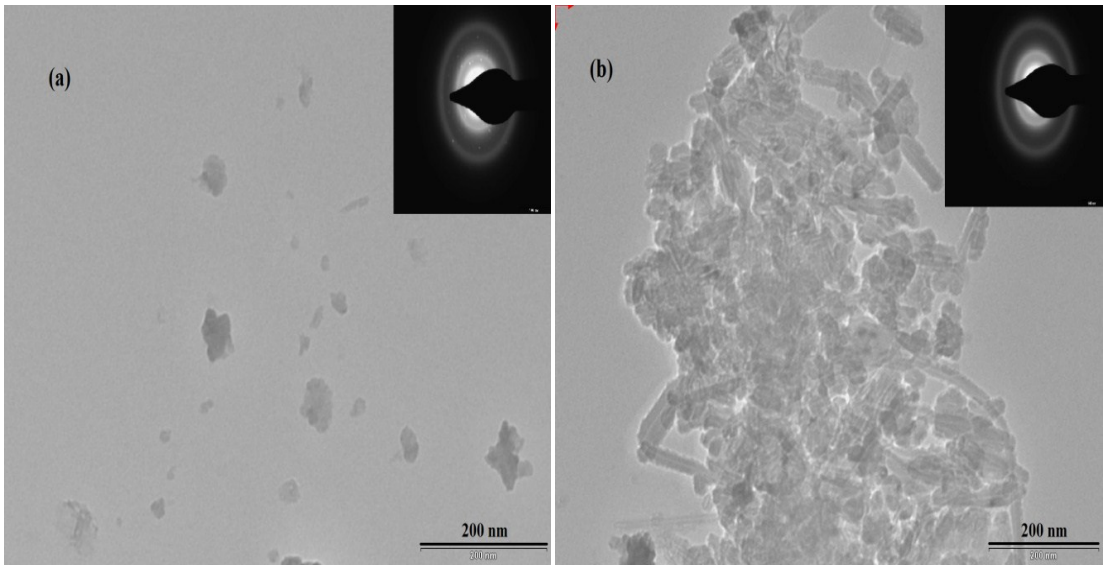

Figure 2A.5 TEM images of (a) undoped ZnS and (b) ZnS:Ni (2.5%) nanoparticles (inset show SAED pattern).

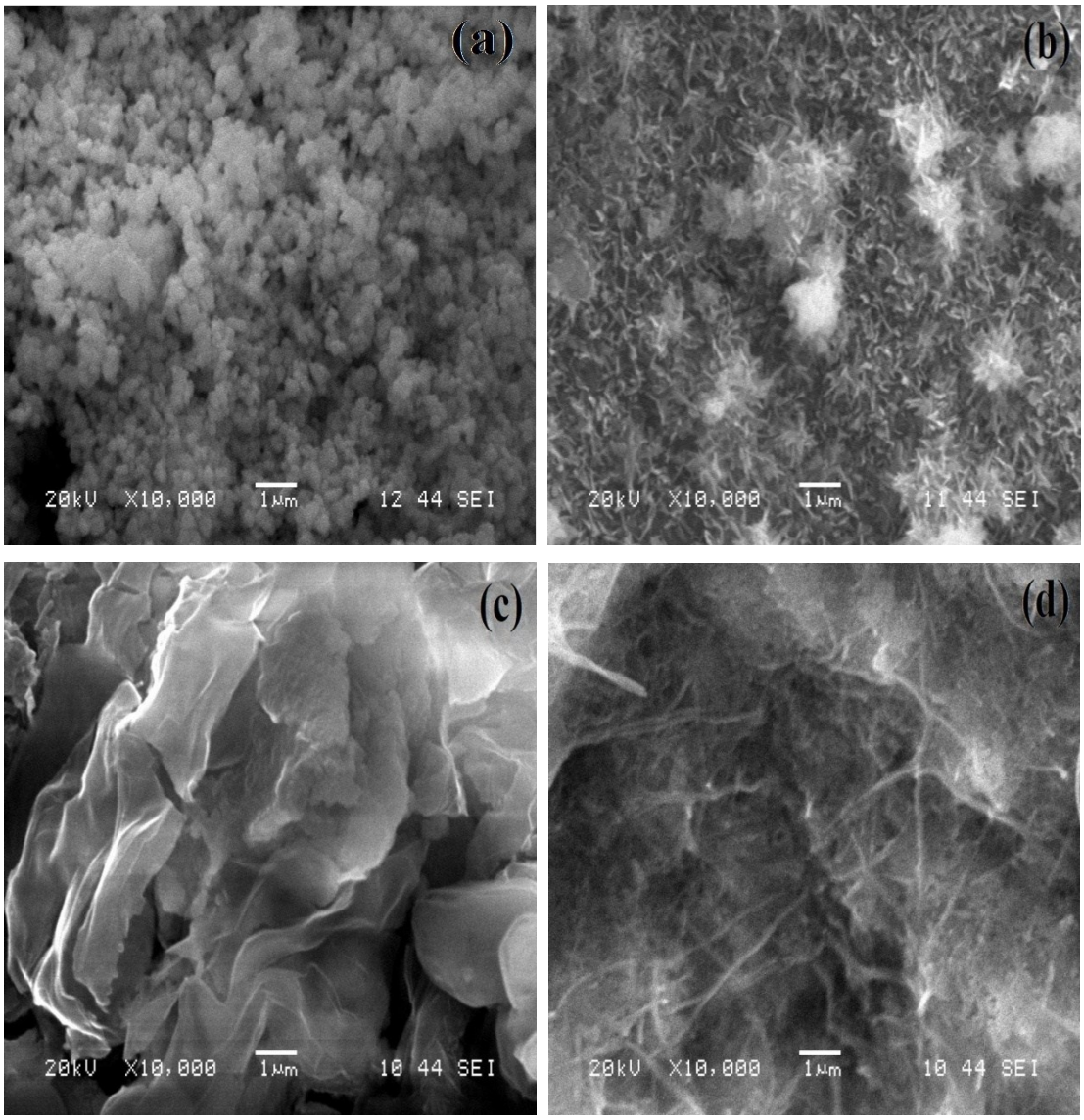

Figure 2A.6. SEM images of (a) ZnS undoped; (b) ZnS:Ni^{2+}(1.2%); (c) ZnS:Ni^{2+} (5.0%); (d) ZnS:Ni^{2+} (10.0%).

We had kept every experimental parameter carefully constant except dopant concentration. So, it was obvious that dopant ions induced 'surface reforming' which resulted in different morphologies. On doping, dopant ions found place either at substitutional sites or interstitial sites of host lattice. Due to differences in ionic radius and electronic parameters, a strain would be created in the host lattice. To relax such strain, the dopants existed in the interstitial sites were ejected towards the surface and those present at the substitutional sites readjusted. This would result in either

‘distortion’ of lattice or ‘complete’ restructuring led to change in morphology. Li et al. reported the formation of nano sheets due to higher concentration (17M) of NaOH which strongly interacted with growing crystal faces and reduced their surface free energies resulting into a retardation of growth from some specific directions and eventually formation of sheet like morphologies [16]. To obtain such morphology, they mixed the required reactants in hydrothermal bomb and heated the same at 230 ◦C and 2.8 MPa pressure.

By such demanding reaction conditions and at higher concentration of NaOH (above 8 M) the interfacial free energy term (IFE) could be made negative and sheet like nanoparticles morphology became thermodynamically spontaneous [17]. It could be understood in this case that OH− ions at such reaction conditions interacted with the growing crystal surface and directed its growth in two dimensions. In our case, similar type of nanoparticle growth behavior was observed but in presence of dopant impurities. As nucleation and crystallization is very delicate process which can be easily disturbed or modified by little changes in experimental conditions like temperature, pressure, pH, capping ligands, presence of impurities etc, one can take advantage of it and direct the growth in a desired fashion. Here, the concentration of NaOH was not high enough and was kept constant throughout the changes but still preferential growth in two dimensions was taking place at 5% concentration of Ni^{2+} and sheet like morphologies were emerged. XRD data also support this. The concentration of Ni^{2+} ions along with capping ligands suppose to direct the growth processes. TheNi^{2+} ions present in solution preferentially interacted with the growing ZnS nanoparticle surfaces having negative charge due to the presence of sulphide ions and capping ligands, also, due to the same reason, interacted and adsorbed to the sides where there were more negative charge through S atom’s vacant orbitals. Thus, there would be a competition between Ni^{2+} ions and ligands to interact with the surfaces with negative charges leading their growth towards minimum free energy.

FTIR spectrums confirm the presence of SH group on the surfaces which sustain this argument. Therefore, crystal growth took place in one direction spontaneously

resulting in a sheet like morphologies (Figure 2A.7). At sufficiently high concentration of dopant ions the crystal growth processes took place in more than one direction with a common centre as shown in the same figure. This argument found further support by our experiment of varying [Ni^{2+}] in the system (0 to 10%) at constant pH. At 10% of Ni^{2+}, the nano sheets (Figure 2A.6d) were transformed to long armed multipods like morphologies. In this case the crystal growth processes hindered and continued to one direction only. This could be due to collection of both dopant impurity and capping ligands to the preferential sites which hindered their growth leading to one dimension nanowires meeting at one junction (Figure 2A.7).

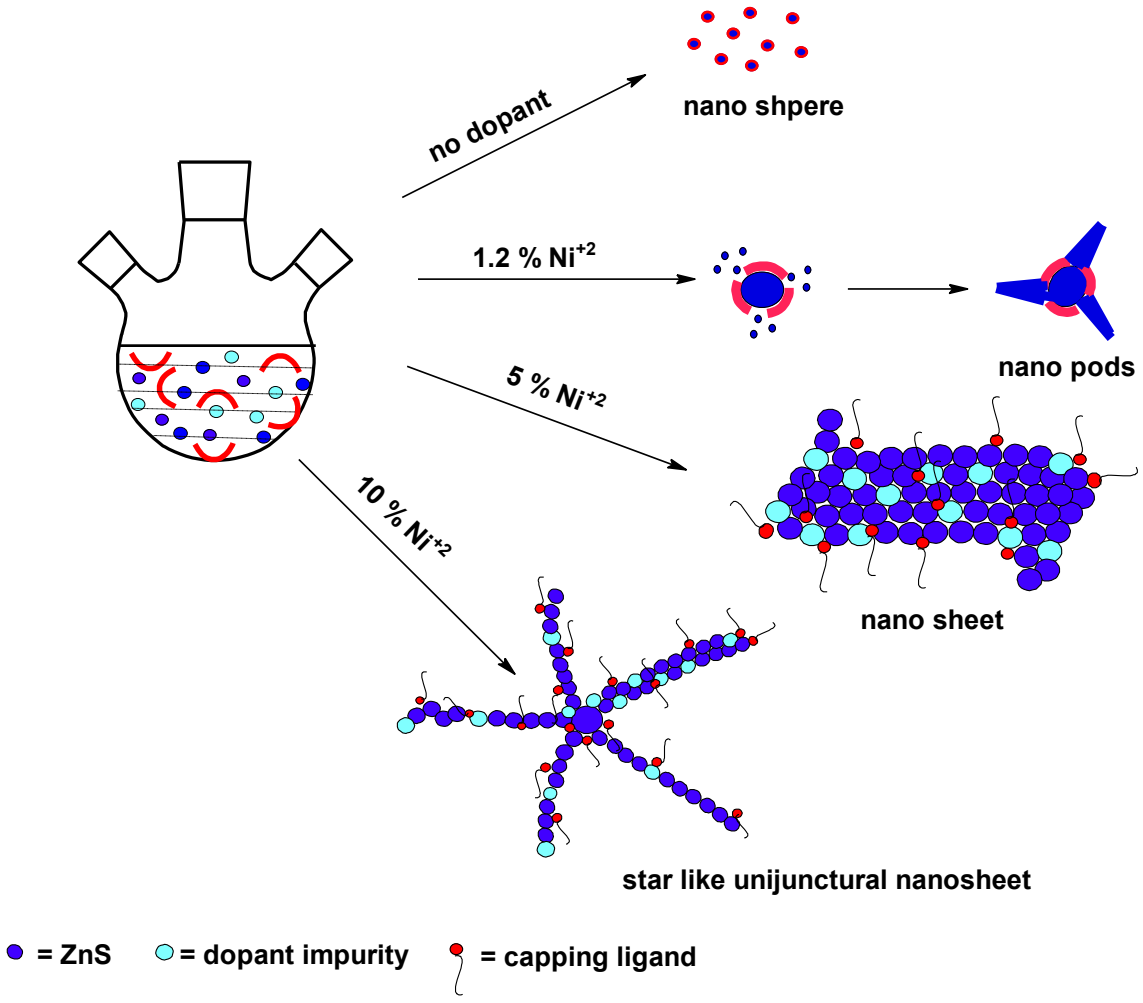

Figure 2A.7. Evolution of different types of morphologies from spherical in presence of Ni^{2+} and capping ligands.

Optical Studies and surface charge stabilization

UV absorption spectra (200 to 400 nm) of ZnS: Ni^{2+} and pure ZnS samples in aqueous solution are shown in Figure 2A.8. The absorption edge displayed a blue shift compared to the bulk ZnS due to quantum confinement [18]. The synthesized nanoparticles showed an increase in band gap when compared with bulk ZnS. The Ni^{2+} doped samples showed absorption spectrum with the shoulder between 285 and 290 nm while the undoped ZnS showed shoulder at 280nm. Thus, by doping Ni^{2+} ions the absorption shoulders are red shifted compared to blank by about 5-10 nm. This is due to the emergence of extra energy levels of dopant ions in the host. It can be seen that the intensity of absorption decreases with an increase in dopant ion concentration. Table 2A.1 lists the estimated band gap values and particle sizes. The particle size was calculated using effective mass model [19] which is in agreement with the size calculated by Debye-Scherrer formulae.

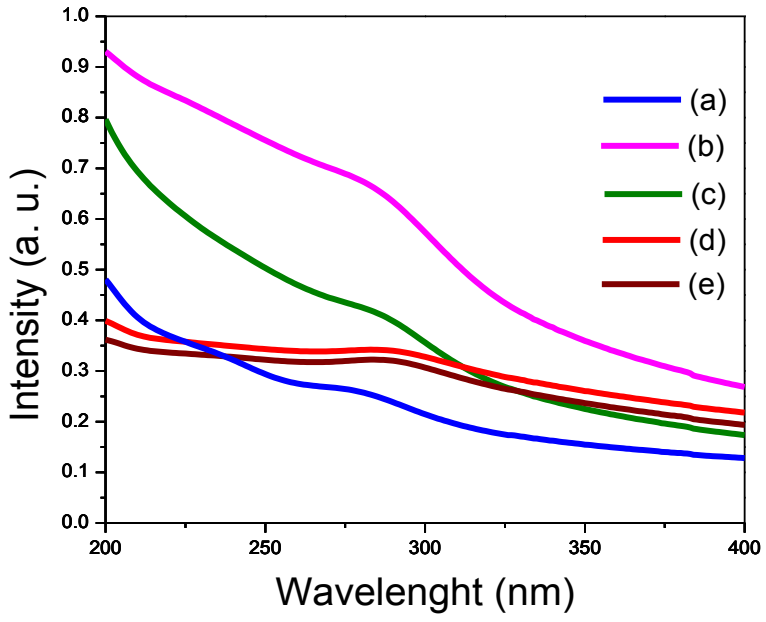

Figure 2A.8. UV absorption spectra of ZnS nanoparticles patterns of ZnS samples: (a) ZnS undoped (b) ZnS:Ni^{2+}(1.2%) (c) ZnS:Ni^{2+}(2.5%) (d) ZnS:Ni^{2+}(5.0%) (e) ZnS:Ni^{2+}(10.0%).

The PL emission of the synthesized ZnS and Ni doped ZnS nanoparticles is studied at room temperature to further investigate the optical properties (Figure 2A.9). An intense peak in violet region at 330 nm is observed due to the defect sites (absence of Zn^{+2} or S^{-2} ions in ZnS lattice sites) in all the samples. Due to the defect sites, the radiative recombination processes between electrons (in conduction band) and holes (in valance band) became intense resulted in a sharp intense peak [20]. Another feature of PL spectra is the intense emission bands in blue region at 422 nm. This may be due to sulfur vacancy and interstitial sulphur lattice defects [21]. From the XRD study it has been observed that both of these emission bands were characteristic features of cubic phase pure ZnS NPs. On doping 1.2% Ni^{+2} ions the intensity of both of these bands decreases. According to Borse et al this behavior was due to the collection of positive charges at the defect sites which intervened the radiative processes [22]. On further increase in concentration of Ni^{+2} ions, the fluorescence intensity at 422 nm decreases and at 10% concentration it is almost quenched. Mainly two factors involved in this study govern the processes of fluorescence. First, the radiative recombinations of excitons at the defect sites and second the type and purity of the phase of host material that is polymorphism. The concentration and nature of dopant ion could directly influence both of these processes. In the beginning, when no dopant ions were present, the ZnS NPs possess cubic close packed structure which is confirmed from XRD (Figure 2A.1). Such NPs can be considered as 'phase pure' and showed the characteristic bands due to the phenomenon explained above. On introduction of 1.2% dopant, the exciton recombination processes were interfered resulted in quenching of fluorescence. However, when concentration of dopant increases to 2.5%, the possibility of trapping Ni^{+2} inside host matrix as well as on the surface of NPs increased. The dopant ions found vacancy either at interstitial sites or at the lattice position replacing Zn^{+2}. This process increases the defect sites and generated new radiation centers resulting in an increase in the intensity of both the bands in fluorescence spectrum (supra vide). EDX data also support this observation.

When concentration of dopant increases to 5%, the fluorescence intensity quenched. From XRD patterns, it could be seen that phase transition began at this point. Now,

the concentration of Ni^{+2} is sufficient to produce a strain in the lattice sites forcing the change of phase in surrounding environment. Thus, both of these phases (mixed phase-predominantly sphalerite cubic along with some hexagonal wurtzite) exist at this concentration. It has been observed that wurtzite phase is more stable at higher temperature [23]. However, the cubic phase is thermodynamically favorable at RT. Thus, if wurtzite phase exists at RT, it requires energy. This can supress the radiative transition processes and hence the low energy radiationless transitions could be favored. 10% concentration of Ni^{+2} induces more wurtzite phase (hexagonal close pack) which further quenches the fluorescence intensity.

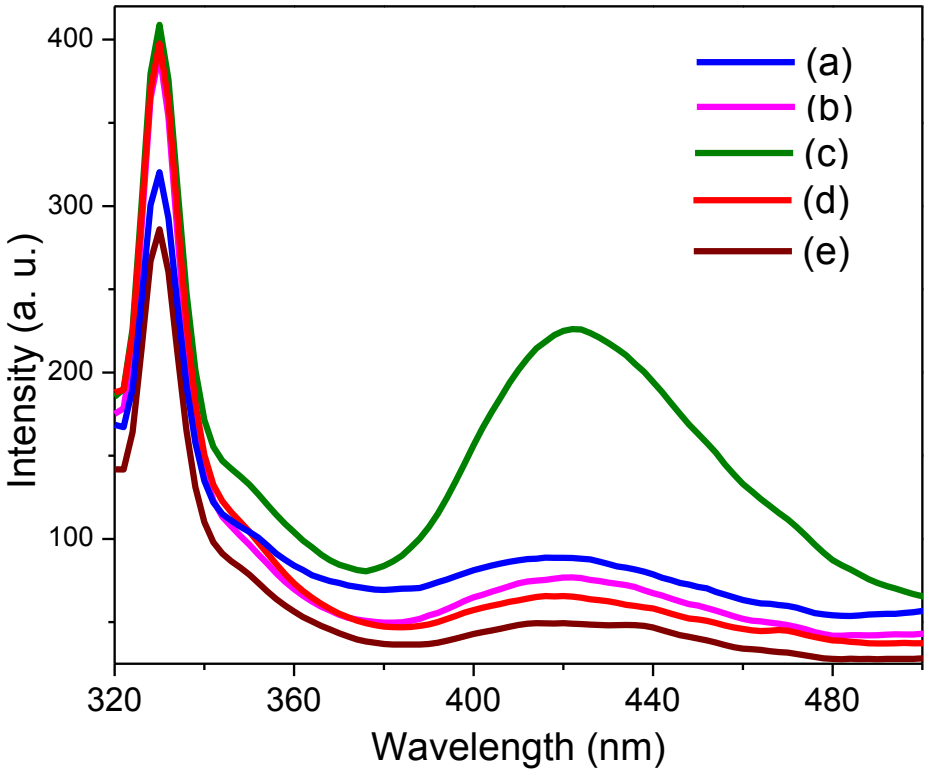

Figure 2A.9. Photoluminescence spectra of (a) undoped ZnS (b) $ZnS:Ni^{2+}$(1.2%) (c) $ZnS:Ni^{2+}$(5.0%) (d) $ZnS:Ni^{2+}$(2.5%) and (e) $ZnS:Ni^{2+}$(10.0%) nanoparticles.

The zeta potential (ζ) was measured in order to gain further insight into the role of surface charge in modifying the luminescence property as shown in Figure 2A.3(f) and Figure 2A.10. It can be seen from the Table 2 that blank ZnS NPs had overall surface charge -28.84 mV. When 1.2% Ni^{2+} ions were introduced, the negative charge decreases which supports our earlier argument for quenching of PL emission. At 2.5% Ni^{2+}, the charge became -29.29 mV. This value of ζ corresponds to electrostatically stable system [24]. Here, Ni^{2+} ions could occupy Zn^{2+} lattice sites more than interstitial occupancy which could result into an overall less charge neutralization and thermodynamically more surface stability responsible for enhancing the luminescence. On introduction of 5 and 10 % Ni^{2+} ions, the surface charge decreased to -14.00 mV. XRD results have shown that at this concentration phase change is occurring. Both of these results led to the belief that at high concentrations Ni^{2+} ions not only occupying interstitial sites (which contributed to neutralize surface charge) but also replacing Zn^{2+} ions from lattice positions. This may create some strains in host matrix with a simultaneous phase change to relax the strain.

In the same line of arguments, the results of Quantum Yield (QY) (Table 2A.2) can be explained. QY represents the efficiency of a material in converting the excitation into fluorescent emission. We have taken blank, with 1.2, and 2.5 % Ni^{+2} dopant ions containing ZnS NPs samples for QY compution. The results are reported in Table 2A.2. It can be seen that the QY of blank ZnS NPs is 11.45% due to absorption of incident photons by defect as well as S^{-2} sites resulting into less fluorescent emission. On doping 1.2% Ni^{+2}, most of the dopant can only be accommodated on the surface (due to less concentration) and passivate the surface. Therefore, the defect sites decreases and also some of the negative charge neutralizes leading to less absorption of incident photons and increase in QY (40.95%). On increasing the amount of dopant ions to 2.5%, now, there is a higher probability of Ni^{+2} ions to diffuse into the crystal lattice and occupy the interstitial sites besides the surface. At these interstitial sites, they may absorb incident photons together with S^{-2} ions present already at some

of such sites. This results into drastic decrease in QY (15.52%) as compared to 1.2% Ni^{+2}.

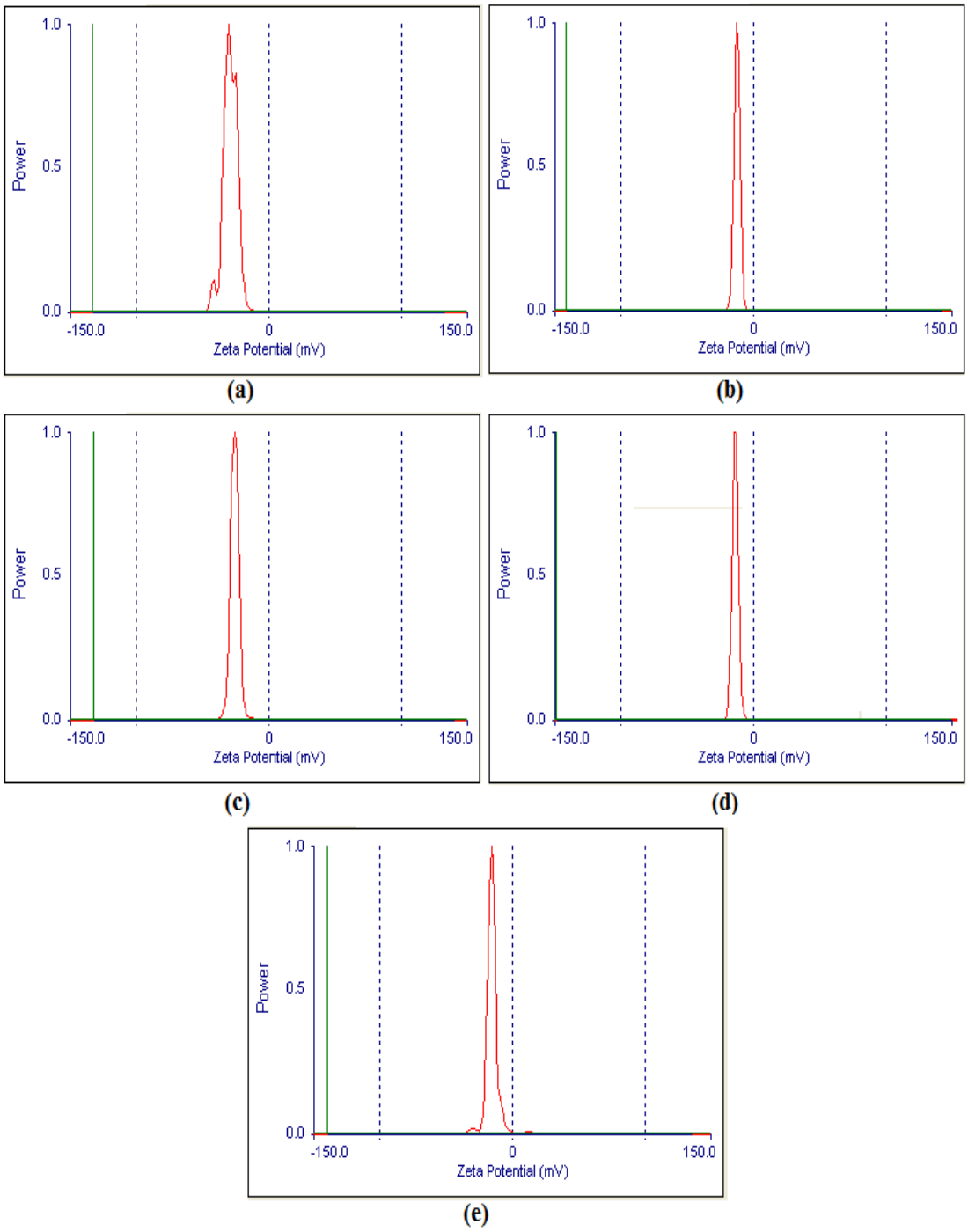

Figure 2A.10. Zeta potential of (a) undoped ZnS (b) ZnS:Ni^{2+}(1.2%) (c) ZnS:Ni^{2+}(5.0%) (d) ZnS:Ni^{2+}(2.5%) and (e) ZnS:Ni^{2+}(10.0%) nanoparticles.

Thermal Study

Differential Scanning Calorimetry (DSC) measures endothermic and exothermic processes in materials as a function of temperature and heat flow. The DSC curves are plotted as a function of heat flow against temperature. Information regarding thermal transitions within the samples such as melting, oxidation, crystallization etc. can be obtained from DSC curves. The DSC curves of blank, with 1.2% and 10% ZnS:Ni^{+2} are illustrated in Figure 2A.11. A broad endothermic peak around 100 ^{o}C as a result of moisture loss is a common feature of all the thermograms. It can be seen from the Figure. 2A.11(a) that for blank ZnS onset of phase transformation from sphalerite to wurtzite occurs above 285 ^{o}C. In case of bulk ZnS this value has been reported around 1020 ^{o}C [25], indicating the transition from bulk to nano regime. Similar exotherm in DSC curve was observed by Tiwari et al [26]. Immediately after phase transformation, the material underwent stress relaxation and endotherm corresponding to 430 ^{o}C suggests the same.

On doping 1.2% Ni^{+2} (Figure 2A.11b), the onset of exotherm shifted down to 230 ^{o}C and continus to 300 ^{o}C, resulting into a broad exotherm. Obviously, this may be due to defects generated by dopant ions causing a strain in the material resulted (a high energy state). Therefore, less energy is required to undergo phase transformation from lower energy state (sphalerite) to higher energy state (wurtzite). The onset of endotherm at 410 ^{o} C indicates stress relaxation due to phase transition and was continued upto 444 ^{o}C. On 10% doping of Ni^{+2} (Figure. 2A.7c), a different pattern of thermogram was observed. Here, the phase transformation took place in steps, initiated at 260 ^{o}C (lower temperature compared to blank), a major exotherm was observed around 350 ^{o}C and continued upto 440 ^{o}C. This could be due to the non-uniform spreading of dopant ions throughout the host matrix produced local pockets of different phases and packing of the same material due to strain. Now more heat and time are required to transform to a new uniform phase, supporting our earlier interpretation.

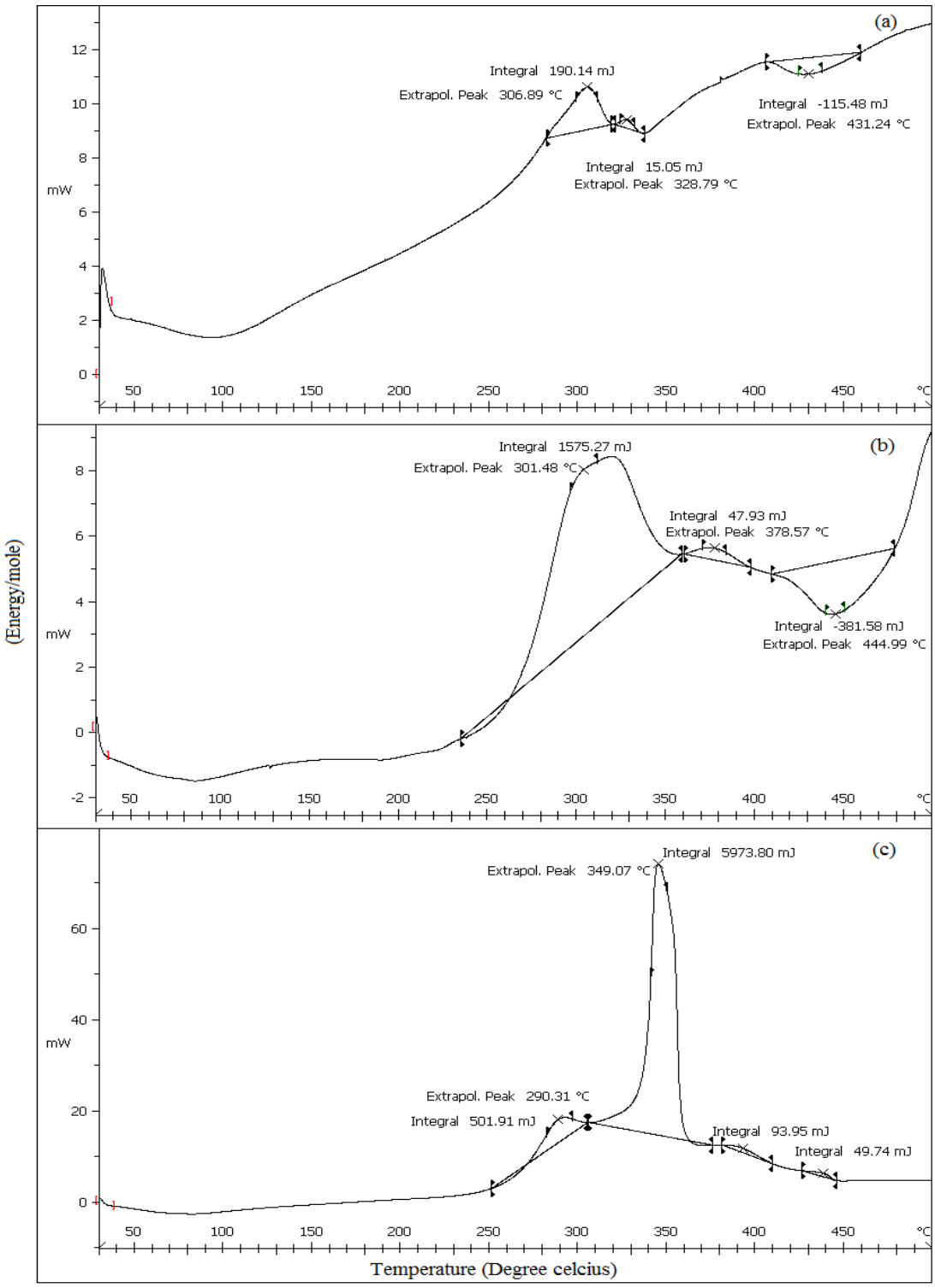

Figure 2A.11. DSC curves of ZnS nanoparticles: (a) ZnS undoped (b) ZnS:Ni^{2+}(1.2%) (c) ZnS:Ni^{2+}(10.0%).

Magnetic study

ZnS is one of the best candidate for Diluted Magnetic Semiconductor (DMS) materials. It was earlier observed that for any material to act as a DMS, a low concentration of dopant ions should be preferred [27]. It was also observed that beyond certain concentration of dopant ions in the host material, the ferromagnetic behavior became weaker [28]. Hence, magnetic hysteresis [M(H)] curve of pure ZnS nanoparticles and those doped with 1.2 and 5.0 % Ni were recorded at room temperature (300 K) to verify their magnetic moments (Figure 2A.12, 2A.13). The curves shown here were obtained after subtracting the diamagnetic background from the sample holder. Coercivity and saturation magnetization (Ms) observed are shown in Table 2A.4. The value of the same Ni nanoparticles has been reported as 49 emu /g. The saturation magnetization observed was much lower than that of Ni nanocrystals. This observation confirms that the origin of magnetism in the samples is not due to presence of reduced magnetic Ni impurities.

It is clear that undoped ZnS nanocrystals show weak ferromagnetic behavior and as the concentration of magnetic ions increases the Ms value also increases. These observations can be explained on the basis of two factors. Firstly, the origin of ferromagnetism in an otherwise non-magnetic solid (on reducing particle size) is due to surface defects [29]. If electrons are trapped in such defects then it serves as an n-type impurity and if holes are trapped then it serves as a p-type impurity which alters the electronic structure of host and induces a new type of magnetism due to orbital coupling. Secondly, as the concentration of 3d transition metal dopant ions increased, the ferromagnetic properties enhanced due to spin-spin coupling which otherwise, in an isolated state produced paramagnetism [30]. It is evident from the PL studies that the number of surface defects increases with the increase in concentration of dopant ion indicating that both of these factors play a role in inducing magnetism in the material. Other factors like electronegativity of atoms of adsorbed molecules on the host surface, charge transfer between ligand and host atoms, presence of unpaired

electrons in ligand atoms, etc., also play an important role for the magnetism in a given material [31]. Besides all of these, the route adopted for synthesis also affects the number of defects and thus, magnetism in the material. To prove this, ZnS nanoparticles (without any dopant) has also been synthesized in pure water medium instead of 1:1 water/methanol. From Table. 2A.4 it could be seen that all the magnetic parameters increased significantly. The most probable reason for such observations is that water being more polar than methanol provides the synergistic effect to orient the magnetic dipole of the dopant ions with the direction of the applied magnetic field resulting in the enhancement of the magnetic parameters.

Table 2A.4. The parameters extracted from the hysteresis loop for ZnS and ZnS:Ni^{2+} nanoparticle.

Sample	Remanence M_r (emu/g)	Saturation M_s (emu/g)	Coercivity H_c (Os)
ZnS undoped	0.0118	0.0272	- 350
ZnS undoped (Synthesized using only water as solvent)	0.0325	0.0486	- 2500
ZnS:Ni^{2+}(1.2%)	0.0086	0.0322	- 500
ZnS:Ni^{2+}(5.0%)	0.0169	0.0397	- 250

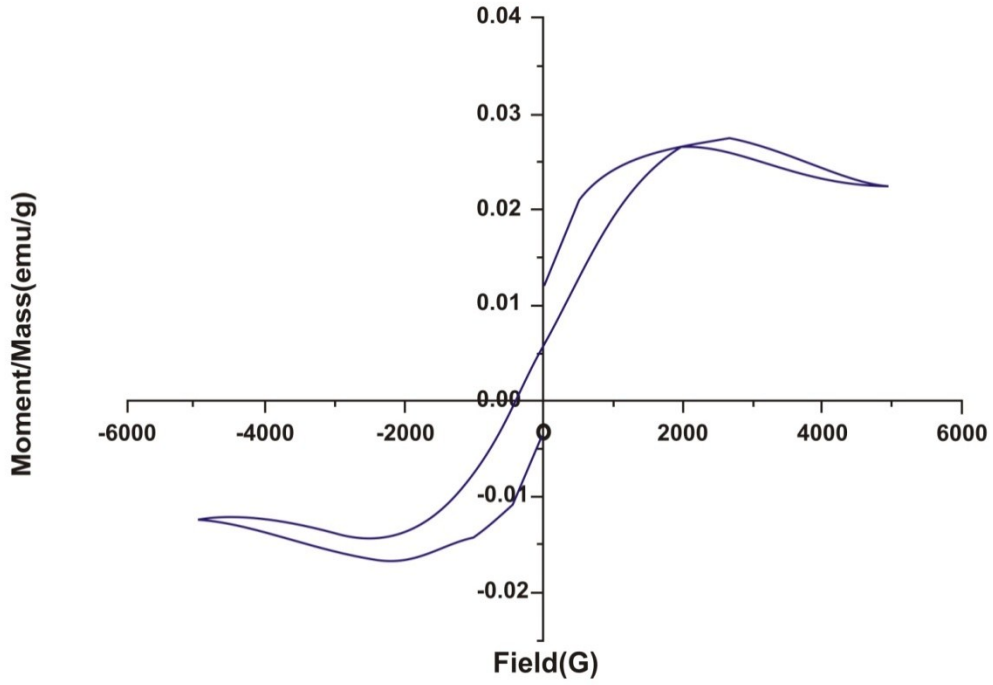

(a)

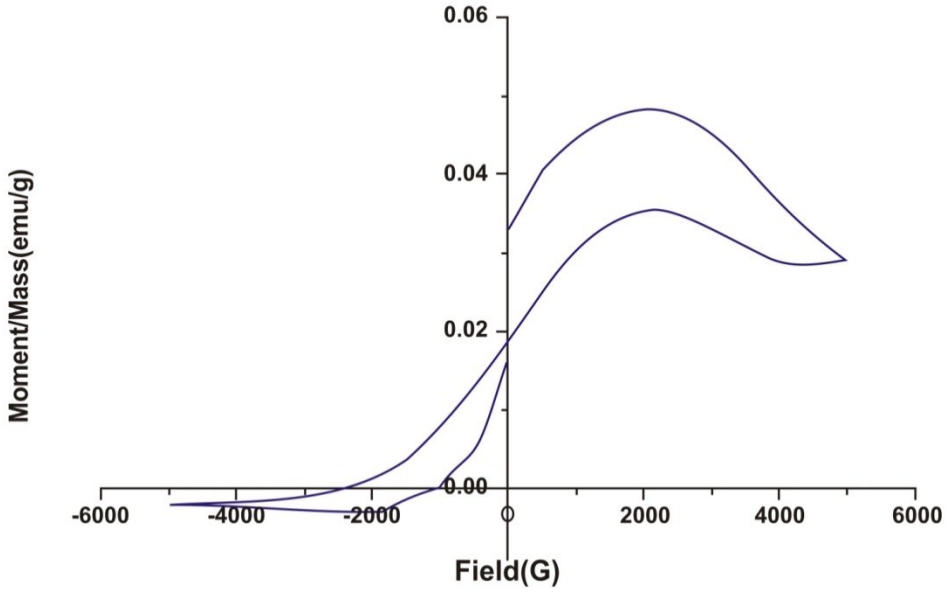

(b)

Figure 2A.12 (b). Fig.12. Magnetic hysteresis [M(H)] curves of ZnS nano particles (a) water/methanol 1:1 mixture as solvent (b) only water as a solvent.

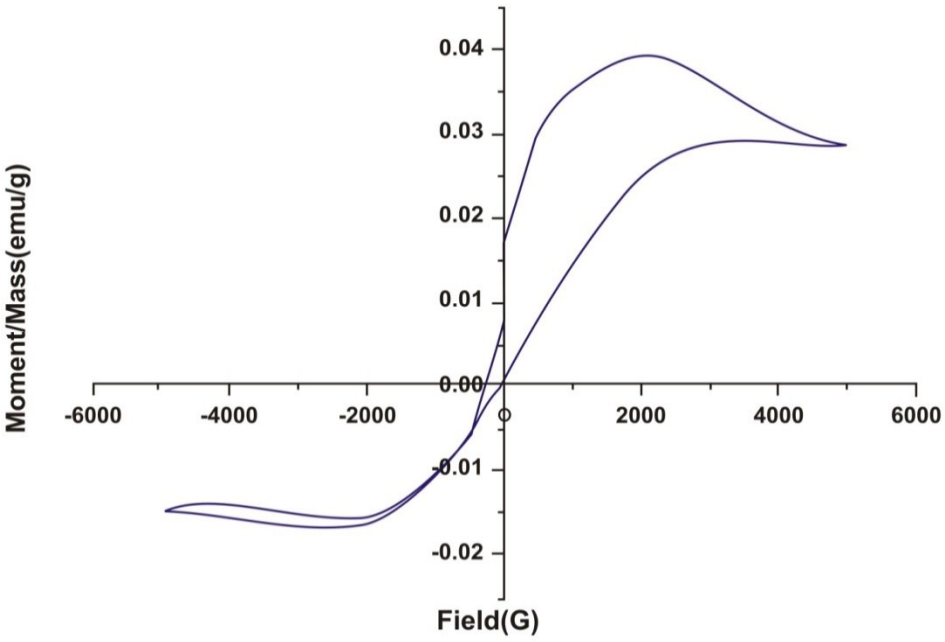

(a).

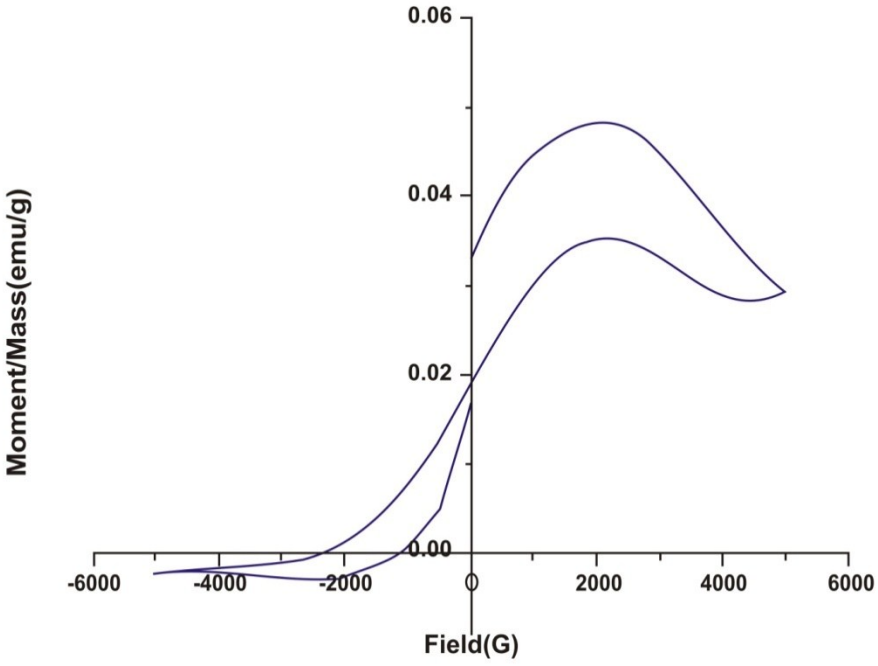

(b)

Figure 2A.13 Magnetic hysteresis [M(H)] curves of ZnS nano particles (a) doped with 1.2% Ni and (b) 5 % Ni at room temperature (300 K).

Conclusion

Ni^{+2} doped ZnS nanoparticles have been successfully synthesized using a simple chemical precipitation method. TEM and SEM study reveal that spherical NPs were obtained in case of undoped ZnS NPs while nano-rods, nano-sheets and long armed multipods were formed in presence of 2.5% Ni^{+2} dopant ions. The present study allows us to conclude: (1) multiple functionalities can be induced in a material by doping as well as varying the dopant ion concentration; (2) while selecting the optimum performance of the material polymorphism plays an important role. Small amount of variation in concentration of dopant ions may leads to changes in the packing of the molecules in host material and change of phase in turn. (3) Ni^{+2} doped ZnS nanoparticles show optimum photoluminescence at 2.5% Ni ion concentration. Thereafter, it is quenched at higher concentration. Thus, purity of the phase together with other factors directly affects the performance; (4) on doping, the number of defects can be increased in a host which directly enhances the magnetism; (5) selecting a proper solvent (or solvent mixture) for synthesis can provide a synergistic effect towards the magnetism and (6) Our experimental observations clearly indicated that it is possible to obtain various morphologies of ZnS nanoparticles by a simple chemical route method without any vigorous reactions conditions. This work opens new possibilities for getting designer nanomaterials with desired properties and morphologies. We have demonstrated that aside from effect of capping agent, the concentration of dopant is one of determinants in the morphology of ZnS nanocrystals.

References

[1] M.Y. Lu, M.P. Lu, Y.A. Chung, M.J. Chen, Z.L. Wang, L.J. Chen, *J. Phys. Chem. C* **2009,** 113, 12878.

[2] G. Li, J. Zhai, D. Li, X. Fang, H. Jiang, Q. Donga, E. Wang, *J. Mater. Chem.* **2010,** 20, 9215.

[3] F. Lu, W. Cai, Y. Zhang, Y. Li, F. Sun, S.H. Heo, S.O. Cho, *J. Phys. Chem. C* **2007,** 111, 13385.

[4] L. Dong, Y. Liu, Y. Zhuo, Y. Chu, *Eur. J. Inorg. Chem.* **2010,** 2504.

[5] J.H. Bang, R.J. Helmich, K.S. Suslick, *Adv. Mater.* **2008,** 20, 2599.

[6] T. Arai, S. Senda, Y. Sato, H. Takahashi, K. Shinoda, B. Jeyadevan, K. Tohji, *Chem. Mater.* **2008,** 20, 1997.

[7] S. Kar, S. Biswas, *J. Phys. Chem. C* **2008**, 112, 11144.

[8] C. Wickleder, *Angew. Chem. Int. Ed.* **2011,** 50, 806.

[9] Y.S. Wang, P.J. Thomas, P.O'. Brien, *J. Phys. Chem. B* **2006,** 110, 21412.

[10] H. Chander, *Mater. Sci. Eng. R* **2005,** 49, 113.

[11] A.P. Alivisatos, *Science* **1996,** 271, 933.

[12] L.E. Brus, *J. Chem. Phys.* **1984,** 80, 4403.

[13] X. Peng, *Acc. Chem. Res.* **2010,** 43, 1387.

[14] R. Jenkins, R.L. Snyder, *Introduction to X-Ray Powder Diffractometry*, John Wiley and Sons, NewYork, **1996**.

[15] R.A. Laudise, A.A. Ballman, *J. Phys. Chem.* **1969,** 64, 688.

[16] D. Li, Z. Lin, G. Ren, J. Zhang, J. Zheng, F. Huang, *Cryst. Growth Des.* **2008,** 8, 2324.

[17] G. Ren, Z. Lin, B. Gilbert, J. Zhang, F. Huang, J. Liang, *Chem. Mater.* **2008,** 20, 2438.

[18] R. Rossetti, R. Hull, J.M. Gibson, L.E. Brus, *J. Chem. Phys.* **1985,** 82, 552.

[19] Y. Kayanuma, *Phys. Rev. B* **1988,** 38, 9797.

[20] A. Goudarzi, G.M. Aval, S.S. Park, M.C. Choi, R. Sahraei, M.H. Ullah, A. Avane, C.S. Ha, *Chem. Mater.* **2009,** 21, 2375.

[21] W.G. Becher, A.J. Bard, *J. Phys. Chem.* **1983,** 87, 4888.

[22] P.H. Borse, N. Deshmukh, R.F. Shinde, S.K. Date, S.K. Kulkarni, *J. Mater. Sci.* **1999,** 34, 6087.

[23] B. Gilbert, F. Huang, Z. Lin, C. Goodell, H.Z. Zhang, J.F. Banfield, *Nano Lett.* **2006,** 6, 605.

[24] J.M. Berg, A. Romoser, N. Banerjee, R. Zebda, C.M. Sayes, *Nanotoxicology* **2009,** 3, 276.

[25] B. Gilbert, B.H. Frazer, H. Zhang, F. Huang, J.F. Banfield, D. Haskel, J.C. Lang, G. Srajer, G. De Stasio, *Phys. Rev. B* **2002,** 66, 245205.

[26] C.S. Tiwary, C. Srivastava, P. Kumbhkar, *J. Appl. Phys.* **2011,** 110, 034908.

[27] D.R.S. Somayajulu, M. Chawda, N. Patel, M. Sarkar, K.C. Sebastian, K. Venugopalan, A. Gupta, *Appl. Phys. Lett.* **2005,** 87, 242508.

[28] P.V.B Lakshmi, K.S. Raj, K. Ramchandran, *Cryst. Res. Technol.* **2009,** 44, 153.

[29] M.A. Garcia, J.M. Merino, P.E. Fernandez, A. Quesada, J. Venta, M.L. Ruız Gonzalez, J. Castro, P. Crespo, J. Llopis, J.M. Gonzalez-Calbet, A. Hernando, *Nano Lett.* **2007,** 7, 1489.

[30] A. Sundaresan, C.N.R. Rao, *Nano Today* **2009,** 4, 96.

[31] D.Y. Inamdar, A.D. Lad, A.K. Pathak, I. Dubenko, N. Ali, S. Mahamuni, *J. Phys. Chem. C* **2010,** 114, 1451.

2B.1 Introduction

Water pollution poses as an acute problem in recent days due to increasing industrialization and anthropogenic activities. Various physical methods such as coagulation, membrane technologies (based on reverse osmosis phenomenon), sedimentation, adsorption etc are in vogue for the purpose. However, the waste gets concentrated at the end of such treatments instead of undergoing complete annihilation [1]. Such concentrated waste is then either incinerated or dumped on land contributing to another type of pollution. The same is true for chemical methods of removal of pollutants using advanced oxidation processes as well. The ground reality is that the available traditional techniques are primitive and unable to eradicate wastes completely by converting them into harmless minerals or gases [2]. Technologies based on innovative ideas are the demand of the day. Solutions to such environmental problems can easily be availed by mimicking the nature. Nature has evolved the techniques such as aerobic and anaerobic degradation of natural wastes by microorganisms using the easily available resources such as water, oxygen, sunlight etc. However, usage of microorganisms to degrade man-made waste is very costly, sophisticated and requires extreme care with regard to the surviving microorganisms given the inconsistent nature of effluent treatment plants. Photosynthesis is a phenomenon that nature has evolved and worth mimicking. In this process, a cascade of multiple events beginning from absorption of photon to generation of oxygen and formation of carbohydrates take place in a precise and synchronized way at multiple centers[3, 4]. At present, we may not be in a position to mimic photosynthesis as a whole but the take home message is that a catalytic system having multiple functionalities can be designed [5]. In a single catalytic system, there should be multiple sites and each should have a predefined function to be performed on receiving signals from the previous process completed at another site. By coordinating the functions at every site, a unique performance from a single catalytic system can be achieved. This concept can be kept in mind in process of designing photocatalyst. In general, photocatalyst is a semiconducting material having a definite band gap between the valance band (VB) and the conduction band (CB). On exposure to an appropriate light source, the electron (e^-) in VB gets excited to CB leaving

behind a hole (h^+) [6].This e^- - h^+ pair collectively is called as exciton. The exciton has a tendency to recombine either radiatively or non-radiatively in femto to nano second time period. The performance of a photocatalyst depends on its ability to break this pair of charge carriers by channeling them to some other pathways before recombination. These isolated e^-s (in CB) and h^+s (in VB) can be then manipulated for other redox processes such as catalytic cleavage of water for hydrogen production, [6, 7] conversion of sunlight into electrical current (solar cell), degradation of pollutants,[8] in the working of field effect transistors for sensors and biomarkers etc [9, 10] and also find applications in new electronics[11] and nano-spintronics[12-14]. The longevity of these charge carriers can be extended by many ways. It is already shown that the charge carriers can be trapped into shallow trap state energy levels near VB or CB or deep trap state energy levels in the bulk of the material [15]. These trapped e^-/h^+ have a thermodynamic tendency to diffuse towards the surface and transfer themselves to the adsorbate at the interface [16].

Another way to achieve better performance is to architect the design of the catalyst as per requirements. Band-gap is one of the important parameters which govern the physical properties of a semiconducting material and it can be tuned by changing the particle size or by introducing impurities (eg. dopant ions) in the material [17]. In the case of photocatalysis, wider band-gap increases longevity of the charge carriers but shifts the light absorption in the UV region which is undesirable. Semiconducting material having (1) sufficient band-gap to make charge carriers separate (2) high surface area, surface defects, different levels of trap states can hold charge carriers longer time (3) active sites at which the substrate can be adsorbed and undergo definite photochemical processes (4) specific mechanism by which the trapped charge carriers can transfer to the active sites and then to the adsorbed substrates (5) tendency to desorb the products formed at the end of reactions from the active sites and (6) capability to be recycled and ready for the new cycle is desired. These functionalities can be achieved by prior designing the catalyst. It was found that active sites around trapped holes show higher activity, stronger binding ability and different dissociation mechanism for the same substrate and product molecules as compared to the active sites around electrons [18].

The first studies of the photochemistry of inorganic particles in aqueous suspension were carried out with ZnS in 1936. It was reported to have the ability of photocalytic decomposition of water [19]. Due to a wide band gap, it absorbs mainly in the UV region, but it can be tuned and shifted to the visible region by doping with metal ions (particularly from transition or lanthanide series). It has been demonstrated that ZnS shows unique catalytic functions due to rapid generation of e^-/h^+ pairs by photo-excitation and the high negative reduction potential of excited electrons [20].

In present study, we have attempted wet chemical synthesis of ZnS NPs with different weight percent of Fe as dopant. Our strategy of designing a photocatalyst is to induce multifunctional sites in the material by doping Fe^{+2}/Fe^{+3} ions. The advantages of our strategy are (1) the band-gap in ZnS can be engineered by reducing the particle size at nano level (quantum dots) making it possible to generate e^-/h^+ charge carriers as separate as possible. (2) Shallow and deep surface states can be generated on varying the amounts of dopant ions. These surface states by acting as 'trap' for charge carriers increase their longevity. (3) The dopant Fe in Fe^{+2}/Fe^{+3} states provides active site to the substrate to be adsorbed by π-metal interaction and (4) The Fe^{+2}/Fe^{+3} system can act as a redox couple and pump the charge carriers from semiconductor to the adsorbed substrates on the surface of nanoparticles. In a previous study we demonstrated that different morphologies can be obtained on varying the amount of dopant [21]. In the present study, we have obtained morphologies like spherical to nano rods having rough surfaces and high surface area. The photocatalytic activity has been evaluated using rhodamine B (Rh B), as a prototype dye, under high pressure mercury vapor (HPMV) lamp and proposed the mechanism of the same.

2.B.2 Experimental

Materials

Analytical grade zinc acetate ($(CH_3COO)_2Zn.2H_2O$), ferrous sulphate ($FeSO_4.7H_2O$), sodium sulphide ($Na_2S.xH_2O$), sodium hydroxide (NaOH) and 2-mercaptoethanol ($HSCH_2CH_2OH$) were procured from Loba Chemie Pvt. Ltd. Mumbai, India.

Rhodamine B was purchased from S D Fine Chemicals, Mumbai, India. All chemicals were used as received.

Synthesis

Aqueous solutions of zinc acetate (0.025 mol) and ferrous sulphate (3.65×10^{-4} mol, for 1.2 % Fe) were mixed with continuous stirring to obtain a homogeneous mixture. During this, the pH of the solution was maintained at 11 using an aqueous solution of NaOH (1M), following drop by drop addition of 2-mercaptoethanol (0.025 mol). Temperature of the reaction mixture, then, was gradually raised to 80 °C and an aqueous solution of sodium sulphide, Na_2S (0.025mol) was introduced drop wise. The mixture was stirred at 10,000 rpm at 80°C for 3h and then allowed to cool naturally. The stirring was further continued for 20 h to obtain homogenous stabilized dispersion. The dispersion was centrifuged at 8000 rpm and the resulting precipitates were washed with distilled water and dried at 60°C. The color of the ZnS:Fe powdered sample was pale brown. Other samples of ZnS:Fe NPs were synthesized by the same method by varying the concentration of ferrous sulphate as 1.463×10^{-3} mol (5.0%) and 2.938×10^{-3} mol (10.0%). Pristine ZnS NPs were also synthesized without using ferrous sulphate.

Evaluation of photocatalytic activity

The photocatalytic activity was evaluated in term of decomposition of an aqueous solution of rhodamine B (with initial concentration of 1×10^{-5} M) under white light irradiation. The white light irradiation was carried out using 250 W High Pressure Mercury Vapor (HPMV) lamp having wavelengths in UV and visible ranges [22]. A specially designed photo-reactor made of double-walled glass tube was used for the purpose. The lamp was placed inside the tube surrounded by circulating cold-water. The whole assembly was kept in another glass chamber containing reactants and a magnetic needle. Subsequently, 20 mL of aqueous solution of rhodamine B (10^{-5}M) was mixed with 50 mg of pristine or Fe doped ZnS (1.2, 5, and 10 % Fe by weight) NPs at RT. The mixture was stirred thoroughly in dark for 60 mins to achieve adsorption equilibrium between reactants on the surface of the catalyst and in the

solution. Thereafter, the solution was transferred to the photo-reactor for HPMV light exposure. At every 2 h time interval, the sampling (3 mL) of the irradiated solution was carried out up to 10 h at RT. At the end, the solution was centrifuged at 10,000 rpm to recover the catalyst and the concentration of RhB present in the solution was determined by using UV absorption spectroscopy.

2B. 3. Results and discussion

X-ray Powder diffraction (XRD)

Figure 2B.1 shows the XRD patterns of pristine and Fe doped ZnS ($Zn_{1-x}Fe_xS$) NPs. The XRD peaks are broad compared to bulk ZnS due to nano regime. Three peaks at 2θ values of 29.06, 48.37 and 57.42 degrees correspond to the scattering from (111), (220) and (311) planes respectively. The XRD patterns for all the samples are well matched with the standard cubic ZnS (JCPDS file No. 65-0309). The calculated d-spacing corresponding to the refraction from these planes are 3.10, 1.90, and 1.62 Å respectively. The lattice parameters a, b and c for cubic structure are calculated as follows:

For cubic system, $a = b = c$

$$d_{hkl} = {}^{a}/_{(h^2 + k^2 + l^2)^{1/2}} \quad \ldots\ldots\ldots\ldots\ldots \quad (1)$$

where h, k and l are miller indices of the peak corresponding to the major refraction planes and d_{hkl} is the inter-planar distance [23]. The calculated values of lattice parameters ($a = b = c = 5.38\ A^o$) for pristine and Fe doped ZnS are same indicating that Fe is well dispersed in the ZnS matrix without distorting the cubic unit cell. On the basis of full width at half maximum (FWHM) of major diffraction peak (111) and Debye-Scherrer formula $D_{hkl} = {}^{0.9\lambda}/_{\beta_{hkl} cos\theta}$ (where D is the average crystallite diameter, λ (= 0.154 nm) is the wavelength of the x-rays, β, the FWHM at diffraction angle θ. The calculated crystallite sizes for all samples are in the range of 2 - 3 nm (Table 2B.1) [24].

From XRD patterns, it can be concluded that (i) all the samples are crystalline in nature and (ii) dopant ions (Fe^{2+} or Fe^{3+}) occupy the lattice sites or interstitial space of the cubic close packed ZnS host matrix and do not form a separate phase as Fe_2O_3, Fe_3O_4 or FeS.

Energy Dispersive X-ray analyses (EDX)

The EDX spectra of ZnS: Fe (1.2, 5.0 and 10.0%) are shown in Figure 2B.2. It can be observed that the diffusion probability of dopant increases up to 5.0% and then saturates at 10.0% concentration of Fe (Table 2B.2). It is possible that the excess Fe may diffuse towards the surface or leach out during synthesis.

Fourier Transform Infrared Spectroscopy (FT-IR)

To ascertain the presence of 2-mercaptoethanol as capping ligand in ZnS nanoparticles, FTIR spectra were taken in the range of 4000-400 cm^{-1} as shown in Figure 2B.3. The obtained spectra were compared with IR of bulk ZnS and 2-mercaptoethanol. From the FTIR spectra the band at 469 cm^{-1} can be assigned to S-S stretching or suphur-oxygen interaction. The bands at 644 cm^{-1} and 651 in ZnS:Fe nanoparticles and undoped nanoparticles can be assigned to the stretching of C-S linkage [25]. Also bands at 1020 cm^{-1} can be assigned to the C-O stretching. The band at 1130 cm-1 was observed in ZnS:Fe nanoparticles can be assigned to S-O stretching vibration due presence of sulphate ions from the iron salt as precursors [26]. This band was absent in undoped nanoparticles. The band at 1414 cm^{-1} and 1548 can be assigned to can be assigned to the symmetric and asymmetric stretching of COO^- respectively from the precursor zinc acetate. The band near 1645 cm^{-1} and 3400 cm^{-1} can correspond to the bending and stretching vibrations of the –OH group. From the FTIR spectroscopy we can confirm the presence of mercaptoethnaol adsorbed on the surface of doped and undoped nanoparticles.

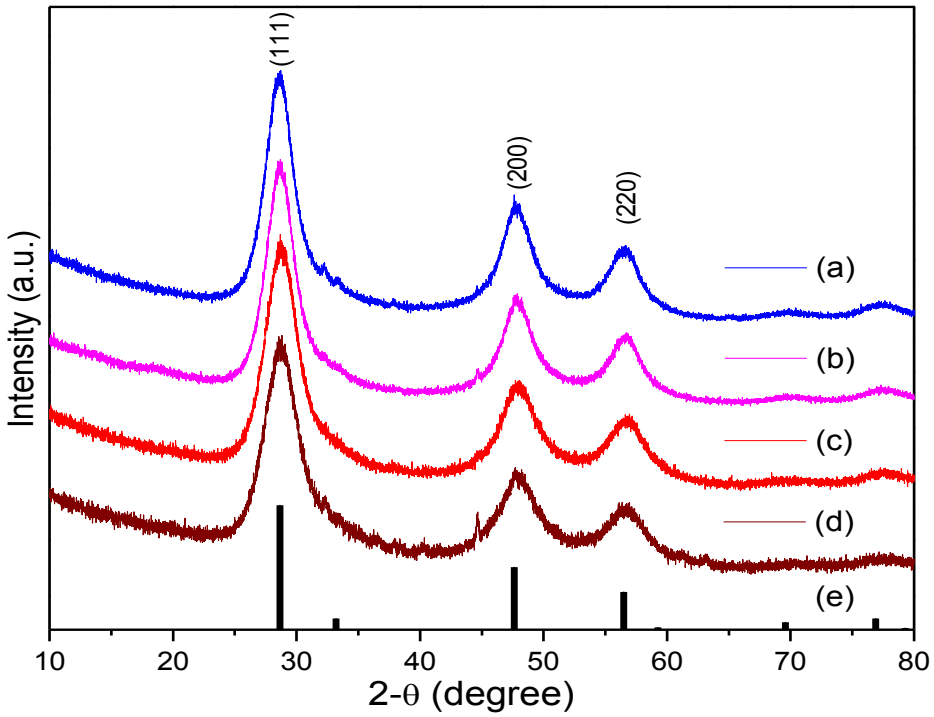

Figure 2B.1. XRD patterns of (a) pristine and with (b) 1.2% Fe (c) 5.0% Fe (d) 10.0% Fe doped ZnS NPs. (e) Bulk ZnS - JCPDS card no. 65-0309.

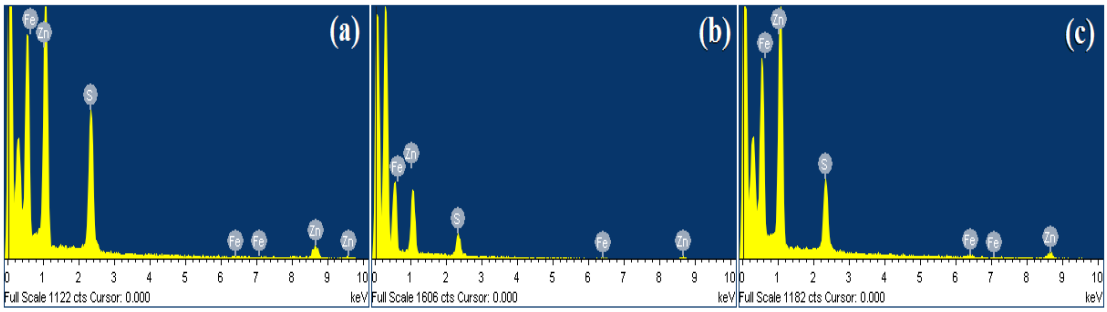

Figure 2B.2. EDX spectrum for (a) ZnS:Fe (1.2%) nanoparticles (b) ZnS:Fe (5.0%) nanoparticles and (c) ZnS:Fe (10.0%) nanoparticles.

Table 2B.1. Particle size (using XRD) and surface charge analysis of ZnS NPS (pristine and Fe doped).

ZnS NPs	Absorption edge (nm)	Band gap (eV)	Particle size (nm)
Bulk	337	3.66	-
Pristine	328	3.78	2.8
1.2% Fe	330	3.77	2.8
5.0% Fe	321	3.87	2.5
10.0% Fe	304	4.09	2.5

Table 2B.2. Elementary composition of the ZnS:Fe^{3+} nanoparticles as studied by EDX.

Sample	at. % of element (Zn)	at. % of element (S)	at. % of element (Fe)
ZnS:Fe^{3+}(1.2%)	48.83	50.80	0.37
ZnS:Fe^{3+} (5.0%)	60.62	36.94	2.44
ZnS:Fe^{3+}(10.0%)	62.85	34.79	2.36

Brunauer-Emmett-Teller (BET) specific surface area (SBET)

The nitrogen adsorption-desorption isotherms for pristine and 1.2, 5.0 and 10.0% Fe doped ZnS NPs, their calculated BET surface area and pore volumes are presented in Figure 2B.4-2B.7 and Table 2B.3. It can be observed from Figure 2B.5 (a) that the isotherm of pristine ZnS NPs is of type I (BDDT classification). The quantity of gas adsorbed, in this case, increases with increase in relative pressure (P/P_o). The hysteresis loop could not be completed on lowering the relative pressure during desorption. This is due to swelling of a non-rigid porous structure or irreversible uptake of molecules in pores (or pore entrances) having the width same as the adsorbate molecules [27]. Doping of Fe influences the isotherm. Isotherms of type IV (BDDT classification) having hysteresis loop of type H_2 in the range of $0.5 < P/P_o < 1.0$ (Figure 2B.4,5) can be observed on doping Fe. The pore size distribution (3.33

nm, Figure 2B.6,7) indicates presence of mesopores in the material. This suggests the presence of pores with narrow necks and wide bodies (ink-bottle pores) in a mesoporous material [28]. It can be observed from Table 2B.3 that on doping, the BET surface area decreases initially, however, it increases gradually on raising the amount of dopant. The BET surface area and pore size studies reveal that the material is competent to exhibit catalytic activities.

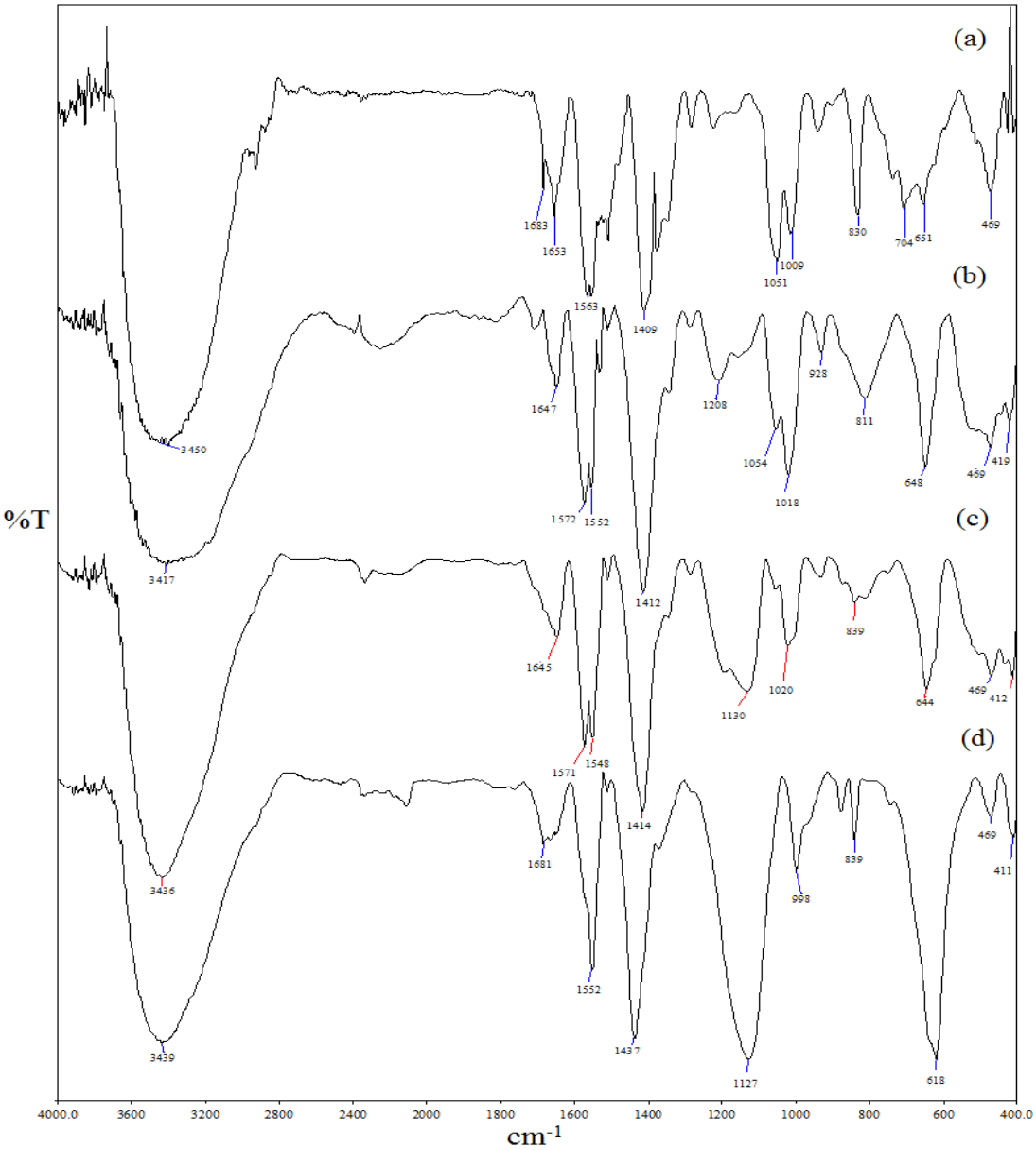

Figure 2B.3. FTIR spectra of (a) undoped ZnS (b) ZnS:Fe (10.0%) (c) ZnS:Fe (5.0%) and (d) ZnS:Fe (1.2%) nanoparticles.

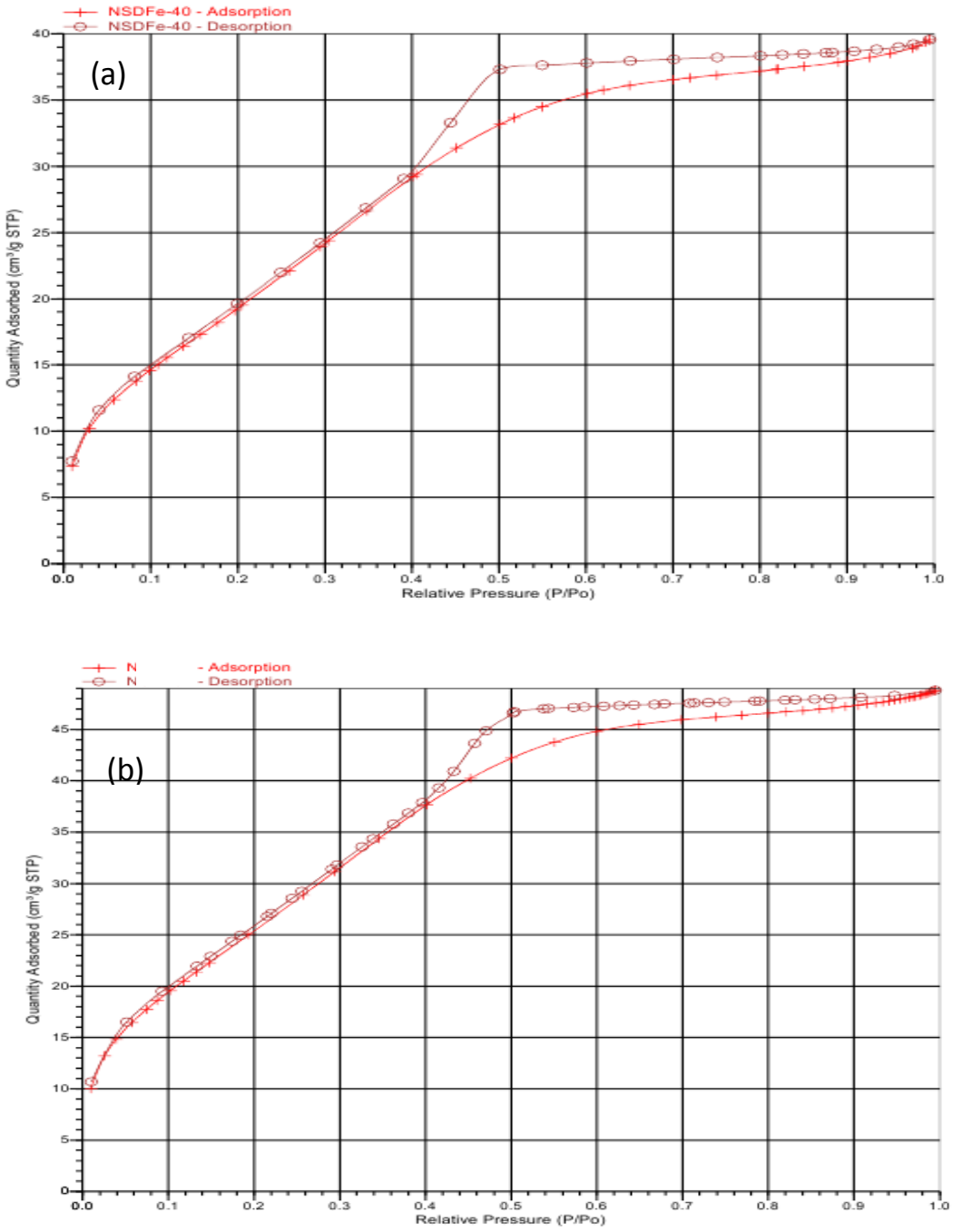

Figure 2B.4. Nitrogen adsorption-desorption isotherms for ZnS NPs with (a) 5.0 % Fe and 10.0% as dopant.

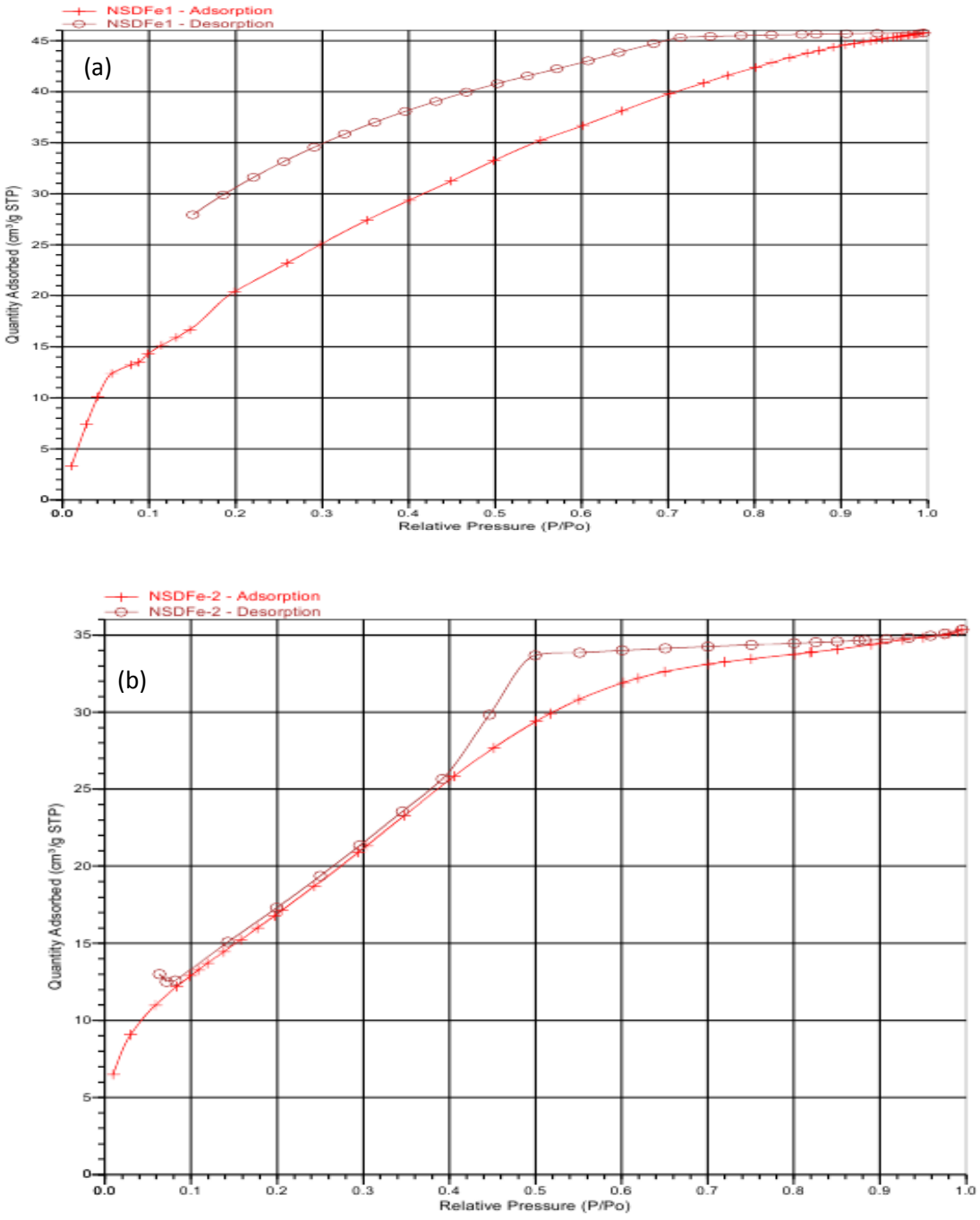

Figure 2B.5. (a) Nitrogen adsorption-desorption isotherms for pristine ZnS nanoparticles (b) ZnS: Fe (1.25%).

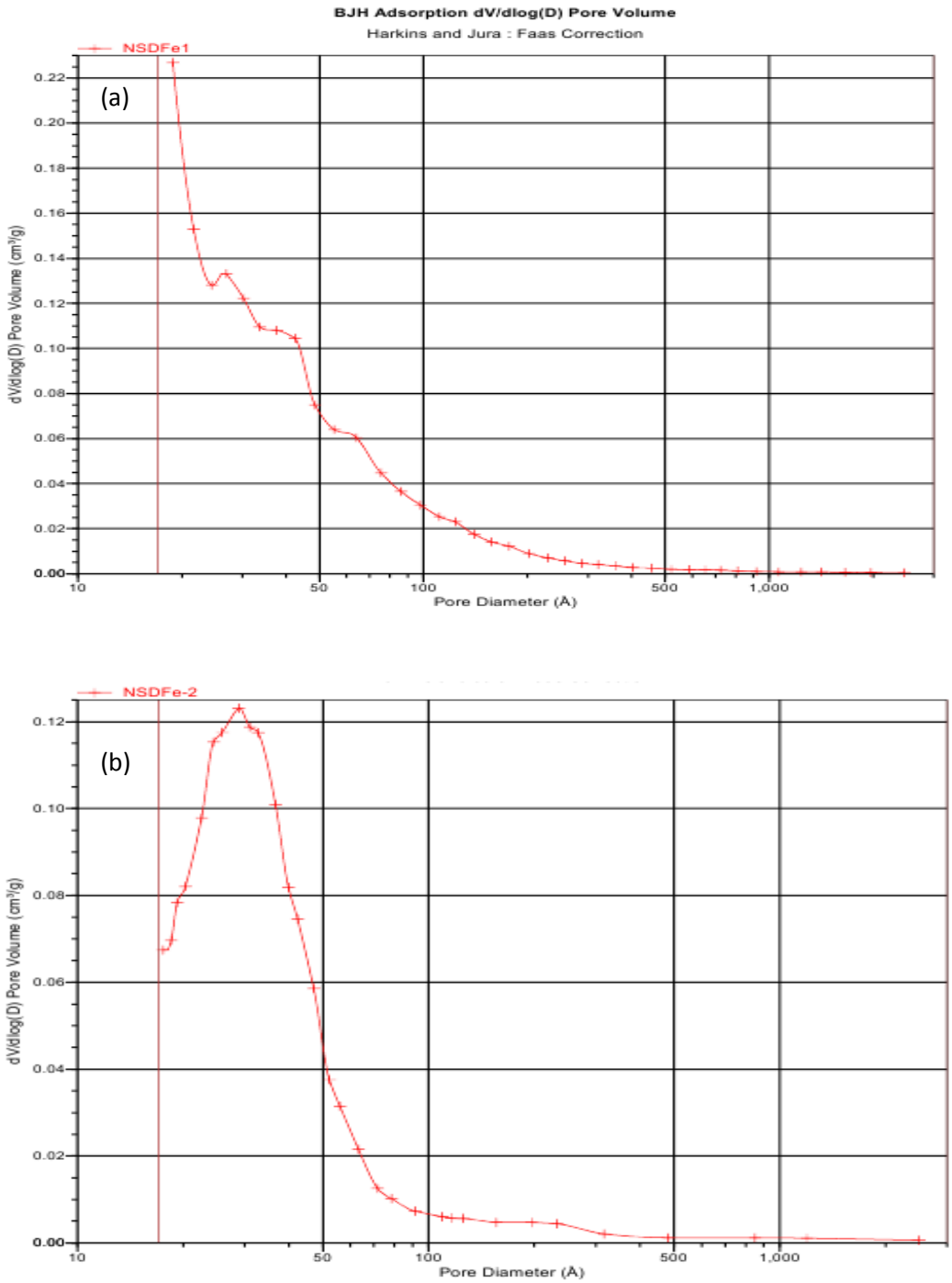

Figure 2B.6. Pore size distribution curves for (a) undoped (e) 1.25% (f) 5.0 % and (g) 10.0 % Fe as dopant in ZnS nanoparticles.

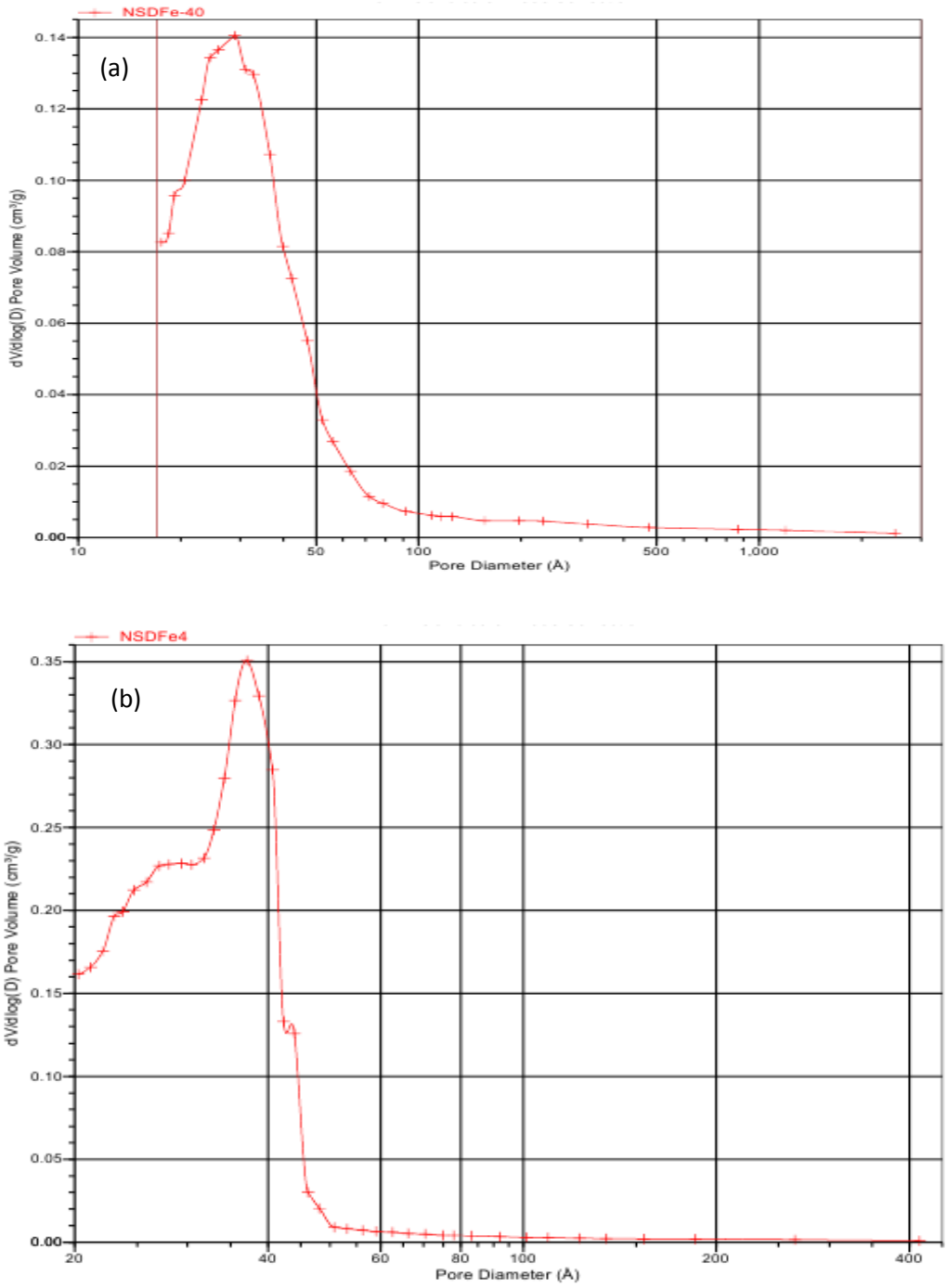

Figure 2B.7. Pore size distribution curves for (a) 5.0 % and (b) 10.0 % Fe as dopant in ZnS nanoparticles.

Table 2B.3. BET surface characterization of ZnS NPs.

Parameters	Pristine	ZnS: Fe (1.2%)	ZnS: Fe (5.0%)	ZnS: Fe (10%)
S_{BET} (m^2/g)	84.93	66.025	75.81	101.42
Average pore diameter (Å)	33.30	33.12	32.29	29.70
Pore volume (cm^3/g)	0.076	0.055	0.061	0.084
Total volume in pores (cm^3/g)	0.065	0.049	0.054	0.067
Total area in pores (m^2/g)	37.37	32.80	37.04	47.33

Transmission Electron Microscopy (TEM)

The morphology of nanoparticles was studied by TEM (Figure 2B.8). The pristine ZnS NPs are spherical and highly crystalline in nature. On doping 1.2% Fe, nanorods with rough surfaces were formed. It can be seen from Figure 3b that these rods having breadth of 88 nm are entangled and highly porous in nature. Zhang et al. proposed oriented attachment-driven ZnO nanocrystals evolving from nanoparticles to nanoplates and eventually to nanowires [29]. On increasing the amount of dopant to 5.0%, the morphology remains the same with increasing length and breadth of rods, ~1.6μm and 109 nm respectively, corroborating the results of BET analysis. Again, nanospheres were formed on 10% Fe doping. In our previous work, we observed similar type of change in morphology with changing the amount of dopant and we proposed the mechanism on the basis of the role of capping ligands and dopants during crystal growth [23]. The SAED analysis confirms the high crystallinity of the material. The HRSEM image of 5% Fe doped ZnS NPs also exhibits the entangled rod like morphology (Figure 2B.9).

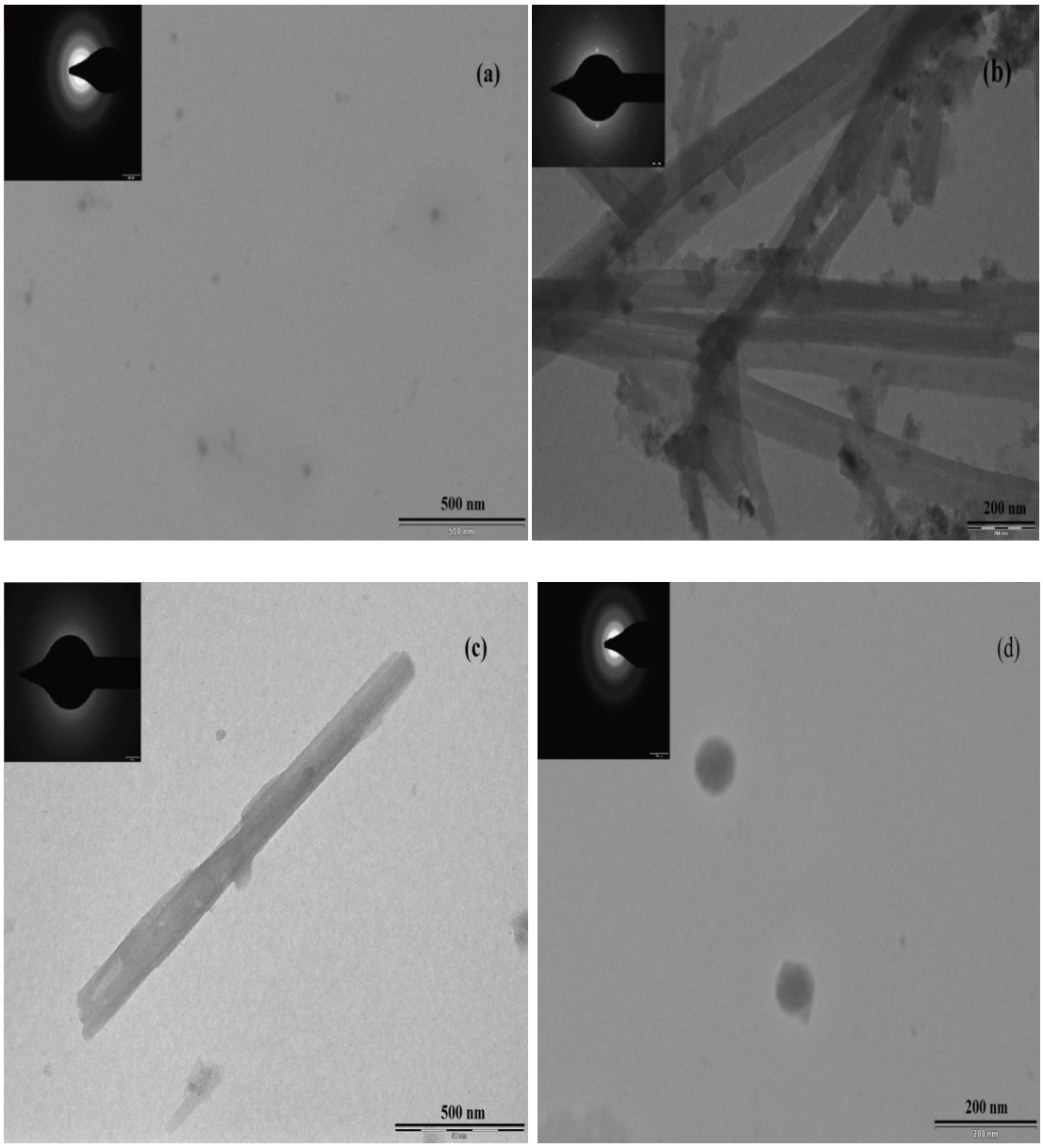

Figure 2B.8.TEM images of ZnS NPs (a) pristine (b) ZnS: Fe (1.2%) (c) ZnS: Fe (5.0%) (d) ZnS:Fe (10.0%). Selected area of electron diffraction (SAED) pattern is shown in inset.

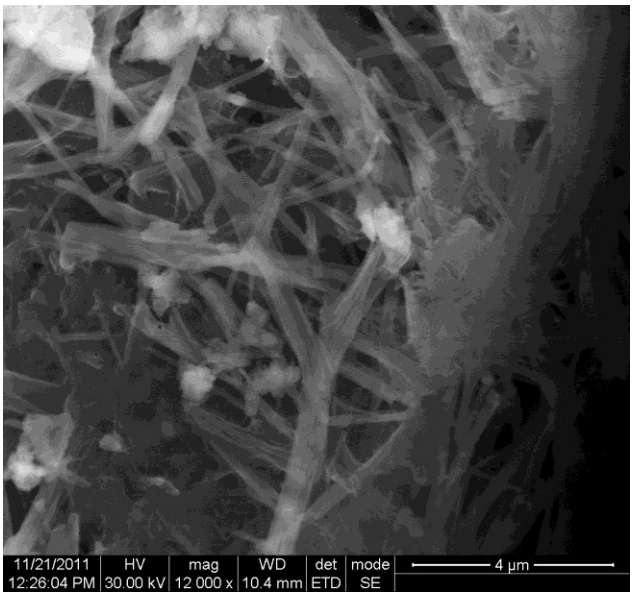

Figure 2B.9. HRSEM image of ZnS:Fe (5%) nanoparticles.

Table. 2B.4. Hydrodynamic diameter and Zeta potential as % doping studied by Dynamic light scateering (DLS).

%Fe	Hydrodynamic diameter (nm)	Zeta potential (mV)
0	556.5	-18.09
1.2	485.3	-21.20
2.5	430.1	-34.84
5.0	227.7	-31.02
10	306.1	-37.13

The diameter of the doped and undoped ZnS nanoparticles were studied by dynamic light scattering (DLS) and its value are given in Table no. 2B.4. In this technique the scattering of light by nanoparticles dispersed in a medium, are correlated with size. The hydrodynamic diameters of doped and undoped nanoparticles were in the range of 200-600 nm as shown in Figure 2B.10. The undoped nanoparticles and nanoparticles with 5.0% doping showed a high degree of monodispersity in comparision to other nanoparticles.

The surface charges of the nanoparticles were studied by zeta potential (ζ) measurement (Table 2B.4). It was observed that electrostatic stabilization of nanoparticles required zeta potential of at least ±30 mV.[30] It can be seen from Table 2B.1 that maximum surface stabilization can be achieved at 5.0% Fe doping in ZnS matrix with charge of -31.02 mV.

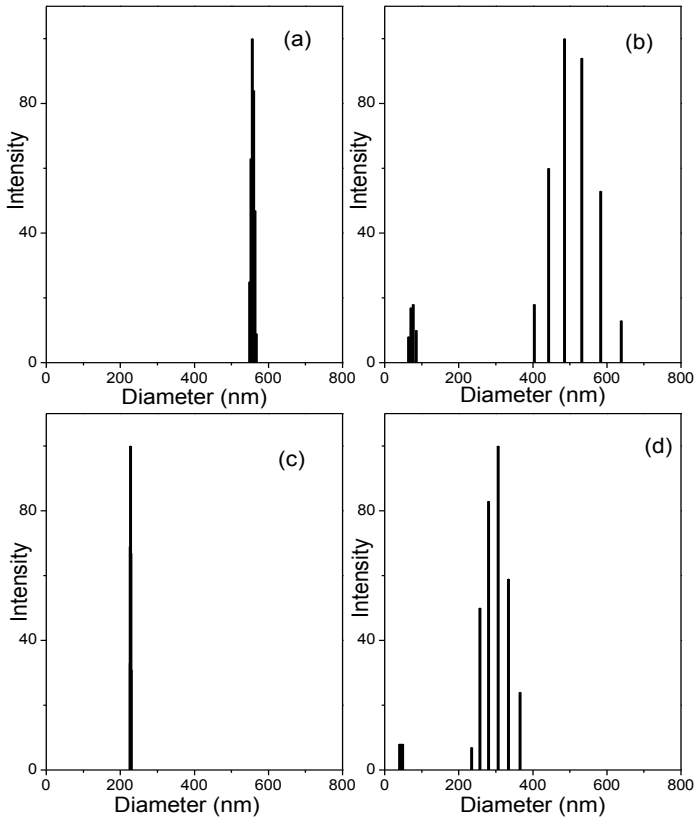

Figure 2B.10. Particle size studied by Dynamic light scattering of (a) undoped ZnS (b) ZnS:Fe (1.2%) (c) ZnS:Fe (5.0%) and (d) ZnS:Fe (10.0%) nanoparticles.

Optical properties

UV absorption spectra provides information about the particle size distribution, energy levels of the valence band (VB) and conduction band (CB), band gap energy etc. UV absorption spectra of pristine and Fe doped ZnS NPs are shown in Figure 2B.11. The absorption edge displayed a blue shift compared to the bulk ZnS due to

quantum confinement [31]. The large blue shifting in the band edge indicates broadening of the band gap and discreteness of the bands. The maximum blue shift can be achieved with 10.0 % Fe doping with rise in the band gap to 4.09 eV (Table 2B.1). This increases the longevity of the charge carriers at room temperature. It can be also observed from Figure 4 that the pristine ZnS NPs show shoulder at 275 nm, on doping it is red shifted in between 285 to 290 nm. This 5-10 nm red shifting is due to emergence of extra energy levels between VB and CB from dopant ions.

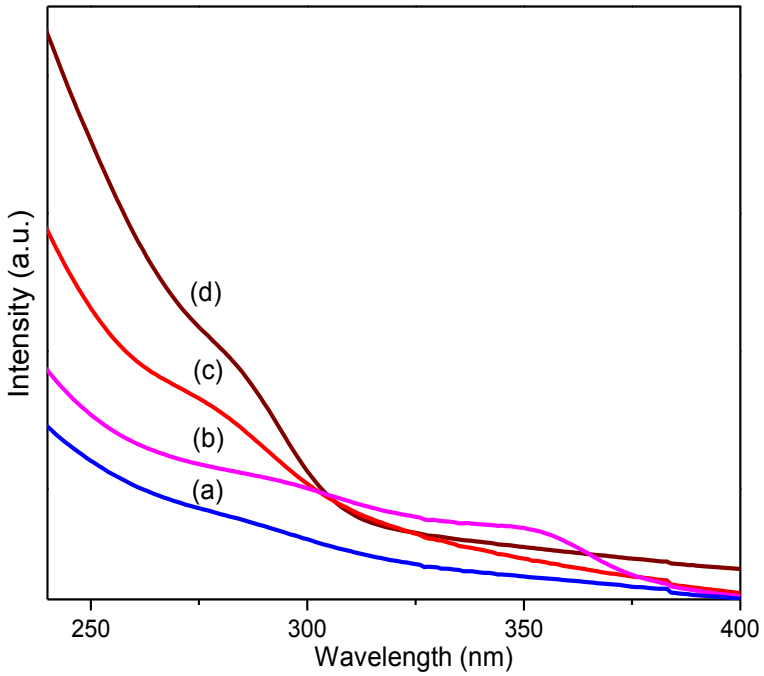

Figure 2B.11. Optical absorbance spectra of ZnS NPs (a) pristine (b) ZnS:Fe (1.2%) (c) ZnS:Fe (5.0%) and (d) ZnS:Fe (10.0%).

The direct band gap energy (Eg) was calculated from a plot of $(\alpha hv)^2$ versus photon energy (hv) using the relationship:

$$(\alpha hv)^2 = A\,(hv - E_g) \qquad \ldots\ldots\ldots\ldots\ldots\ldots\ldots\ldots (2)$$

Where, $(h\nu)$ is the photon energy, and α, the absorption coefficients (α = 4πk/λ, k is absorbance, λ is wavelength in nm), and A, constant. The E_g was determined by extrapolating the straight line portion to the hν-axis (Table 2B.1, Figure. 12) [32]. It can be observed from Table 2B.1 that the direct band gap energy remains almost constant up to 2.5% Fe doping. Then the E_g value notably increases in the case of 5.0 and 10.0% doping. This observation can be explained as follows: as the particle size decreases, the energy levels of VB and CB become more discrete resulting in increased E_g.

Photoluminescence (PL) is one of the important techniques to study the charge carrier dynamics and photo-physical processes occurring at molecular level. It also gives information about defects and traps that exist in the material and their interaction with charge carriers [33, 34]. Figure 2B.13 shows the PL spectra of ZnS NPs with and without dopant at the excitation wavelength of 290 nm. It can be observed that on excitation, multiple emission processes get initiated. We had proposed the division of emission spectrum into two, crystallinity dominated and defect dominated regions [35].

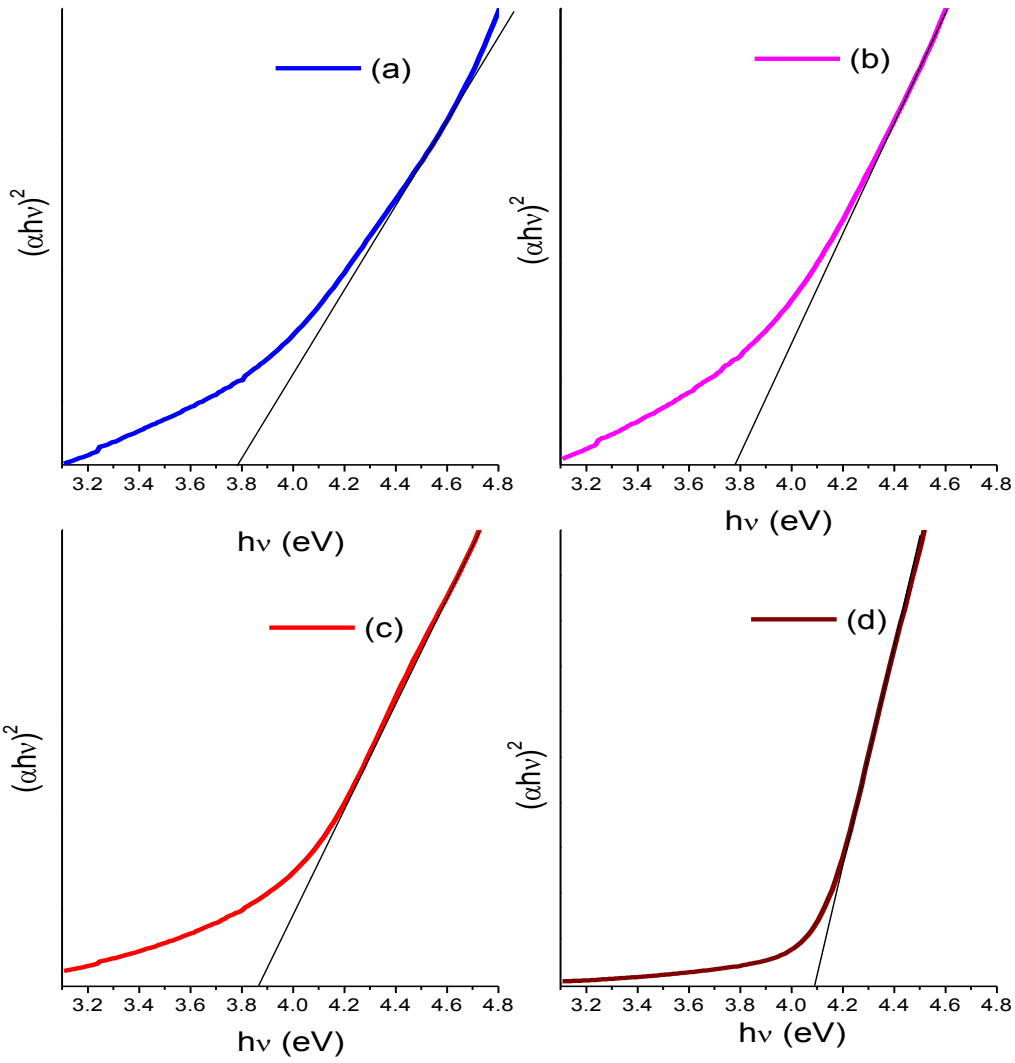

Figure 2B.12. Plot of $(\alpha h\nu)^2$ vs hν of (a) pristine ZnS nanoparticles (b) ZnS:Fe (1.2%) (c) ZnS:Fe (5.0%) and (d) ZnS:Fe (10.0%).

In pristine ZnS NPs, the broad band to band emission peak is blue shifted to around 330 nm on doping Fe ions. This indicates filling of Zn vacancies and increase in crystallinity of the material. The 400 nm onward spectral region can be considered as defect dominated region which throws more light on charge carrier dynamics due to defects. In ZnS host, large numbers of energy levels just below the CB are formed due to sulfur vacancies (Vs) [36]. Such energy levels or vacancies act as traps for electrons and also as donor centers. On the contrary, Zn vacancies (V_{Zn}) and cationic

dopant impurity generate energy levels above the VB of ZnS host. These energy levels or impurity centers act as hole trap and also as acceptor centers. In pristine ZnS, the emission at 410 nm is due to charge carrier recombination from Vs to VB, whereas at 460 nm it is due to transfer of electron from Vs to V_{Zn}. The emission at 490 nm indicates the presence of excess Zn ions on the surface [37]. Now, on doping Fe, either in Fe^{2+} or Fe^{3+} state, these photo-physical processes get modified due to extra energy levels and defects are introduced from dopant as an impurity. It can be seen from Figure. 2B.13 that on doping with Fe, the emission at 410 nm due to transition from V_{Zn} to VB is almost quenched while that at 460 nm due to Vs to V_{Zn} decreases in intensity indicating trapping of charge carriers or increase in charge carrier density.

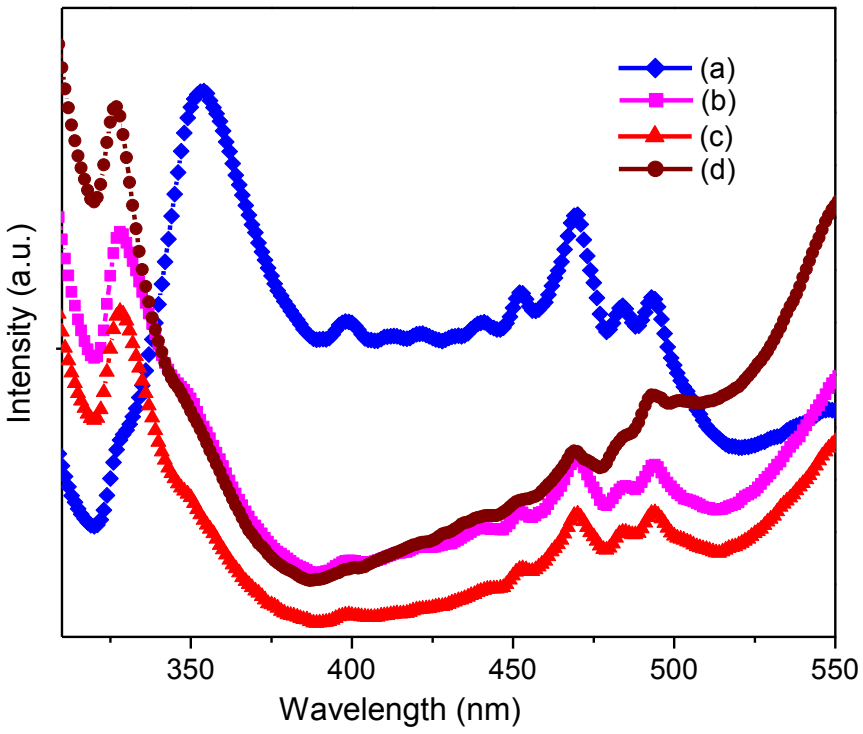

Figure 2B.13. PL spectra of ZnS NPs (a) pristine (b) ZnS:Fe (1.2%) (c) ZnS:Fe (5.0%) (d) ZnS:Fe (10.0%).

Photocatalytic performance of pristine and Fe doped (1.2%, 5.0% and 10.0%) ZnS NPs were evaluated by studying the absorption spectra of the same in RhB solution in terms of change in intensity of λ_{max} at 545 nm. RhB was used as a test contaminant and an indicator of photocatalytic activity of all synthesized samples. The percentage degradation efficiency of samples was calculated (Equation 3). Pure RhB dissolved in water shows only 12.5% degradation (due to presence of ·OH free radicals generated from water) in 10 h when irradiated under HPMV Lamp. Figure 2B.14 shows time dependent UV-vis absorption spectra of RhB solution during photo-irradiation in presence of pristine, 1.2%, 5.0% and 10.0% Fe doped ZnS NPs at every 2 h time interval. The decreasing intensity of the dye solution (λ_{max} centered at around 554 nm) indicates the degradation of dye with time. It is interesting to note that besides decreasing the intensity of the peak, it becomes broad with little blue shifting. According to Wu et al. this is due to degradation of dye into small fractions causing elevation in energy needed for the movement of electrons [38]. The $ln\,{C_o}/{C}$ Vs time plot indicates maximum rate constant can be achieved in case of 5.0% Fe doped ZnS NPs (0.2069 h^{-1}) with 93.06% degradation of dye. Absences of any other absorption peak in the visible spectra manifest complete degradation of dye. It can be observed that photocatalytic degradation of RhB follows first order kinetics, as all curves are straight lines and intercept near the origin on the y-axis. The % degradation with calculated rate constants is presented in Table 2B.5. It is obvious from the results that photocatalytic degradation efficiency of ZnS NPs increases at 5.0% Fe dopant level (Figure. 2B.16, 2B.17). After three photo-degradation cycles of RhB, the catalyst did not show any significant loss in its activity implying efficient recovery and recycling of the catalyst at the end of reaction.

The percentage degradation efficiency of samples was calculated as

$$\% \text{ efficiency} = 100 \times [A_o\text{-}A]/A_o = 100 \times [C_o\text{-}C]/C_o \quad (3)$$

Where $A_o(C_o)$, and A (C) are initial absorbace (or concentration) and absorbance (or concentration) after irradiation at various time intervals respectively.

Photocatalyst works by two mechanisms (i) by direct adsorption of dye pollutants on its surface to transfer the photo generated charge carriers and (ii) by generating ·OH or $O_2^{\cdot -}$ free radicals from the decomposition of water or reaction of e^- with H_2O_2 generated in a cascade of reactions (Scheme 2) [39- 43]. As ·OH is a strong oxidizing agent (E^o = +3.06 mV) it oxidizes the dye pollutant almost completely. Here, we propose the rational approach of designing the photocatalyst in such a way that both mechanisms can be operational.

Table 2B.5. Degradation of aqueous solution of RhB dye under white light irradiation after 10h.

% Fe	% Degradation	Rate constant (h^{-1})
0	89.80	0.1915
1.2	88.74	0.1821
5.0	93.06	0.2069
10.0	77.56	0.1309
without catalyst	12.56	0.0044

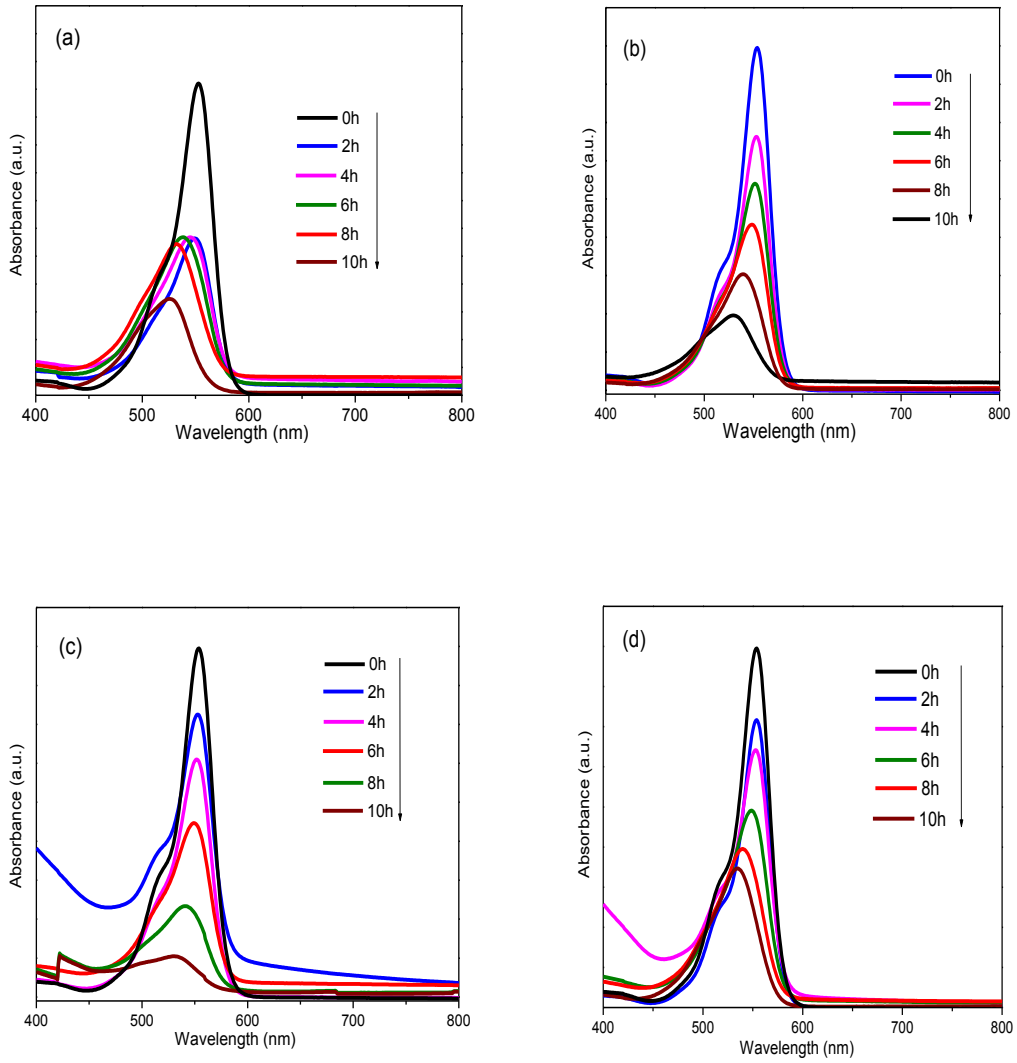

Figure 2B.14. The photocatalytic degradation of RhB dye in terms of diminishing intensity of λ_{max} at 554 nm in presence of (a) pristine (b) 1.2 % Fe (c) 5.0 % Fe and (d) 10.0 % Fe doped ZnS NPs.

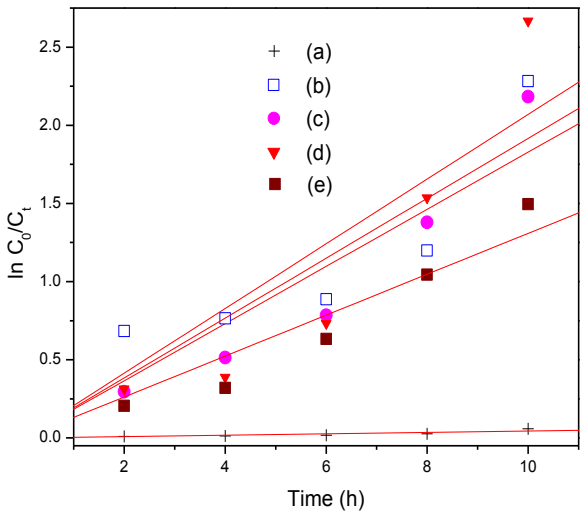

Figure 2B.15. Photo-degradation of RhB under HPMV irradiation (a) without any catalyst; in presence of (b) pristine (c) 1.2% Fe (d) 5% Fe and (e) 10% Fe doped ZnS NPs.

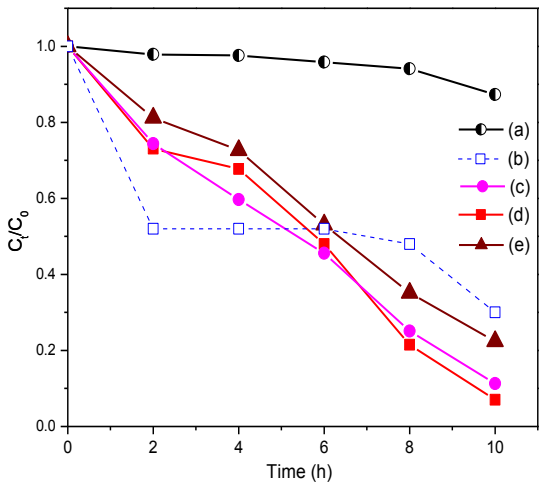

Figure 2B.16. Photodegradation of RhB under HPMV irradiation in precence of (a) without any catalyst (b) pristine ZnS (c) ZnS:Fe (1.2%) (d) ZnS:Fe (5.0%) and (e) ZnS:Fe (10.0%) .

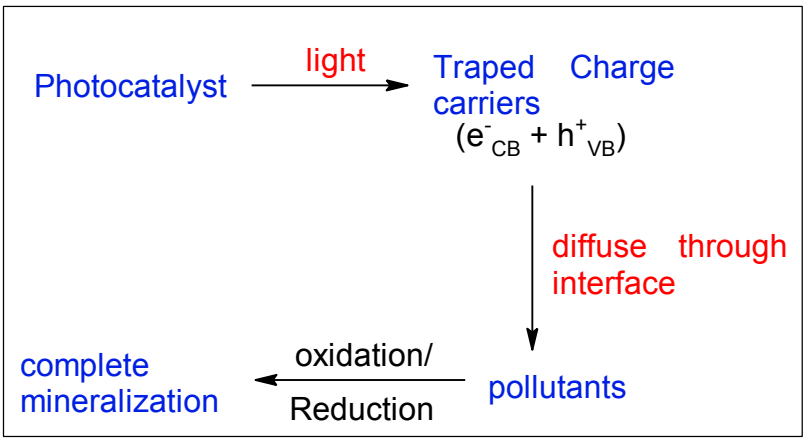

Scheme 1. Schematic of direct degradation of dye pollutant on the surface of photocatalyst.

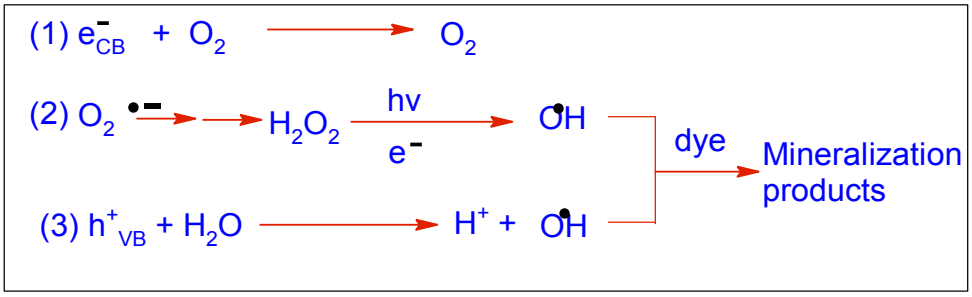

Scheme 2. Hydroxyl free radical mediated photocatalytic degradation of dye.

We believe that the catalyst works by utilizing first mechanism when dopants are present by coordinating with organic molecule by π-metal interaction. Shallow surface states near CB can be constructed which can trap the charge carriers and increase their longevity. This can be achieved by doping with Fe ions. To confirm the participation of ·OH free radicals in the photocatalytic processes, the PL spectra of illuminated basic solution of terephthalic acid in presence of pristine and 5 % Fe doped ZnS NPs at different time intervals were recorded (Figure 2B.17). The PL intensity at 425 nm increases with irradiation time in presence of ZnS:Fe and the pristine ZnS NPs (Figure 2B.18). This observation confirms that ·OH actively takes part in the degradation of RhB dye [44, 45].

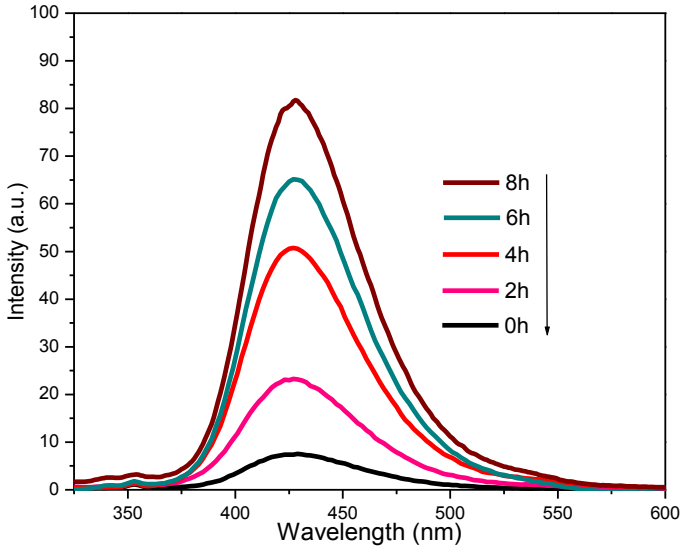

Figure 2B.17. PL intensity of basic solution of terephthalic acid under HPMV irradiation at different time intervals in presence of ZnS: Fe (5.0%) NPs.

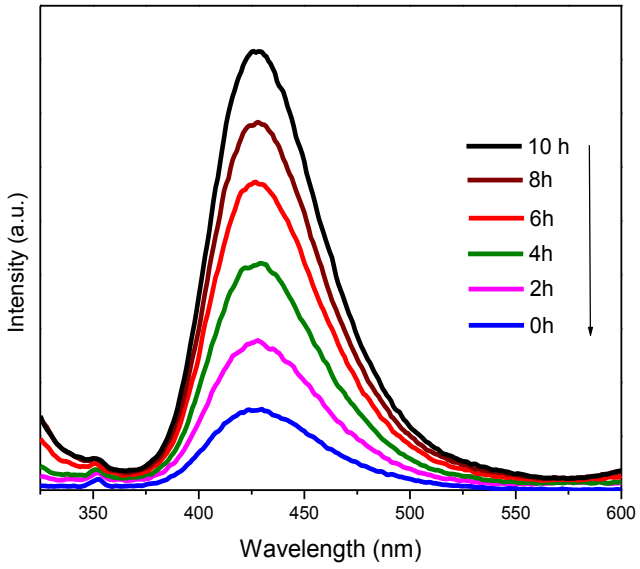

Figure 2B.18. PL intensity of basic solution of terephthalic acid under HPMV irradiation at different time interval in precence of undoped ZnS nanoparticles.

Mössbauer spectroscopy

The location of dopant ions, their interaction with the surrounding as well as their oxidation states play critical role in the functioning of catalyst. Mössbauer spectroscopy is one of the tools to characterize local composition and structure of the catalyst having Fe as dopant ions [46]. Figure 2B.19 shows the Mössbauer Spectra of the $Zn_{1-x}Fe_xS$ samples for x = 0.012, 0.05 and 0.10 concentrations. The spectra were least square fitted with standard fitting program with parameters listed in Table 2B.6. The best fitted data present two quadrupole doublets. The two doublets are attributed to two sites in ZnS matrix, site A and site B with splitting of 0.83 and 0.52 mm/s respectively. These two doublets and isomer shift support the presence of Fe^{3+} (site A) and Fe^{2+} (site B) charge state indicating superparamagnetic nature in small crystallites. The Fe^{2+} charge state is due to the Fe present in substitutional sites of Zn^{2+} in ZnS matrix. However, Fe^{3+} charge state is due to nearby cationic vacancies (Zn or S). The FWHM for both the sites are ~1.3 times that of line width of the spectrometer suggesting that a unique environment is present around Fe. The XRD spectra also support our fitting. It can be observed from quadrupole splitting (QS) that with increase in concentration of Fe, the sites B population decrease i.e. Fe^{2+}/ Fe^{3+} ratio decrease. This increases the charge carriers in the ZnS matrix. It can be summarized from the Mössbauer spectral analysis that Fe is uniformly distributed in the matrix with Fe^{3+} excess in the higher level concentration samples. Fe interacts with its surrounding such that its magnetic moment quenches at RT otherwise hyperfine splitting would be observed in Mössbauer spectra [47]. This indicates that Fe does not form any local magnetic phase such as FeS, Fe_2O_3, Fe_3O_4 in the host.

Magnetic properties

However, the material shows weakly ferromagnetic behavior at RT in VSM analysis and the saturation magnetization values increase with rise in concentration of Fe (Figure. 2B.20 and Table 2B.7). VSM analysis gives information about bulk magnetism of the material which is weakly ferromagnetic in this case.

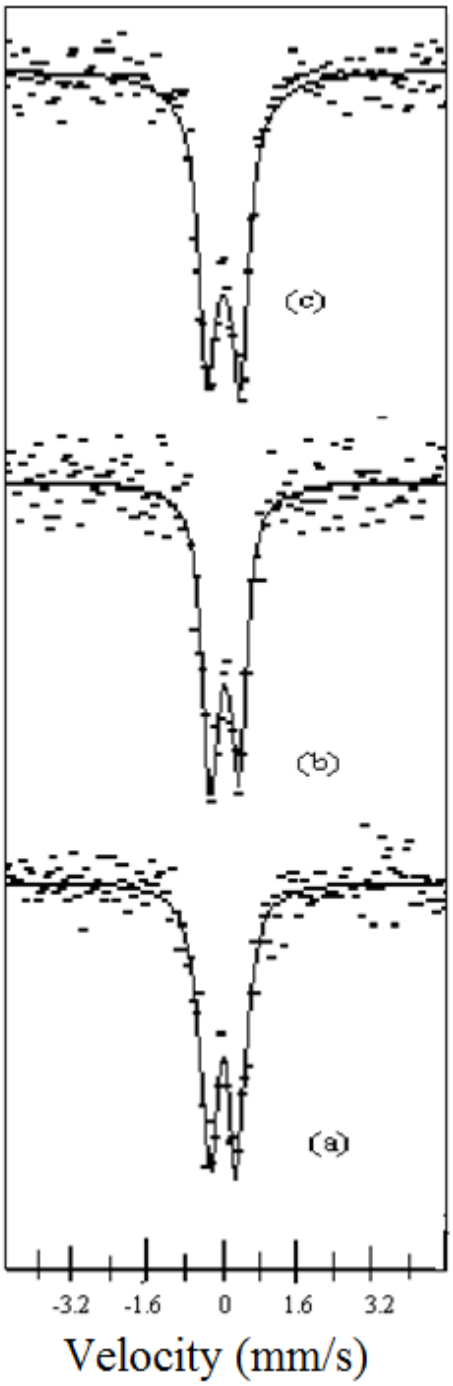

Figure 2B.19. Mössbauer spectra of ZnS NPs with (a) Fe (1.2%) (b) Fe (5.0%) and (c) Fe (10.0%).

Cyclic voltammetry (CV)

To understand the effect of dopant ions and redox behaviour of the material electrochemical analysis were performed. Cyclic voltammetry (CV) is one of the best tools for the purpose. The CV curves (Figure. 2B.21) show the cathodic current at negative peak potential and it can be observed that ZnS NPs reduced during negative scan [48]. Upon addition of salt of Fe^{2+} the additional peak appears during oxidation scan at -0.77 V corresponds to standard oxidation potential for Fe^{2+}/Fe^{3+} vs NHE. On increasing the amount of Fe^{2+} upto 5% the intensity of anodic current peak (positive current) and cathodic current peak (negative current) increases indicating both oxidation and reduction take place respectively during the opposite scans in the material. At 10% dopant (Fe^{2+}) level, the intensity of anodic current becomes higher and that of cathodic current lower suggesting oxidation of Fe^{2+} to Fe^{3+} favoured. From the cyclic voltammograms and Mössbauer spectroscopy it can be assumed that there should be equilibrium between Fe^{2+} and Fe^{3+} amount in the material. As the amount of Fe^{2+} increases during synthesis, the amount of Fe^{3+} also increases leaving an electron in the material. Hence, the concentration of electrons should be increased with the dopant ions and it directly affects the nature of the conductivity of the material.

Mott-Schottky (MS) and electrochemical impedance spectral (EIS) study

Mott-Schottky (MS) and electrochemical impedance spectral (EIS) measurements were carried out by using the impedance techniques to find out the origin and fate of charge carriers in the material [49]. As described earlier, the synthesized ZnS NPs form a mesoporous material and hence the electrolyte can penetrate through the voids easily [50]. The reciprocal of capacitance vs applied potential curves were plotted using the MS equation [51] as:

$$\frac{1}{{C_{SC}}^2} = \frac{2}{\varepsilon\varepsilon_0 N_d A^2}\left[(E - E_{FB}) - \frac{kT}{e_0}\right] + \frac{1}{{C_H}^2} \qquad (4)$$

Where C_{Sc} is the space charge capacity, ε, dielectric constant of ZnS, $\varepsilon_{0,}$ the electric permittivity in vacuum, $e_{0,}$ the elementary charge constant, $N_{d,}$ the donor density, A, surface area, k, Boltzmann constant, T, the absolute temperature, E, the electrode applied voltage, E_{fb}, the flat band potential and $C_{H,}$ the Helmholtz capacitance. The donor density (N_d) was also calculated from the slope of the linear region using the equation:[51]

$$N_d = -\left(\frac{2}{e_0 \varepsilon_0 \varepsilon}\right)\left(\frac{d(1/C^2)}{dE}\right)^{-1} \qquad (5)$$

Figure 2B.22(a) shows the Mott-Schottky curves of the pristine ZnS and Fe doped ZnS NPs film as working electrode in 0.1M KCl solution. It can be observed that the reciprocal of capacity of semiconductor follows a linear function with applied potential. This characteristic shows the n-type nature of semiconductor. However, as the amount of dopant increases, the slope of the straight line decreases indicating the increase in donor concentration on the electrode surface due to defect levels (Table 2B.8.). The flat-band potentials (E_{fb}) was calculated on extrapolating the straight lines to x-axis ($1/C^2 = 0$). The E_{fb} values vs. Ag/AgCl and equivalent to vs. NHE are reported in Table 2B.9. The E_{fb} of Fe doped ZnS shows a negative shift in comparison to pristine ZnS. We know that in n-type semiconductor, the E_{fb} is equal to the Fermi level (E_f) and very near to conduction band (differing 0.1-0.3 ev) [52]. The reduction potential of Fe^{+3}/Fe^{+2} is 0.77 V (vs. NHE) which is very much positive than the conduction band potential E_{cb} of ZnS NPs (-1.72 V against NHE) facilitating the transfer of electron from the conduction band to dopant energy levels under incident light, from where it is easy to capture by molecular oxygen to convert into $\dot{O}_2^-$ during the degradation of RhB dye. From the MS plot, the energy level diagram was constructed [53- 55] (Figure. 2B.22b). It can be seen that the enhancement in band gap energy shifts the light absorption to near uv region (UV-A which is not absorbed by the ozone layer and form 5% of the sunlight); however, it is compensated by dopant energy levels between VB and CB of the host material. This is the case upto 5% Fe dopant level. After that the band gap is shifted to UV-B region of shorter wavelength. The presence of excess donors (Fe^{2+} or electrons trapped in defects) strengthens the capacity of the material as a reducing agent. Overall, it can be

concluded from the MS analysis that Fe as a dopant enhances the electron density in the material increases n-type conductivity and makes the material stronger reducing agent.

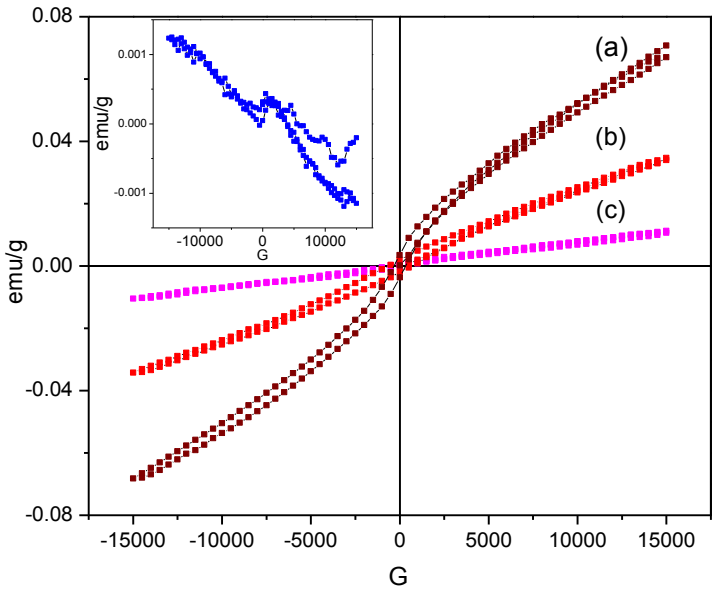

Figure 2B.20. The VSM hysteresis curves for (a) Fe (10.0%) (b) Fe (5.0%) and (c) Fe (1.2%) doped ZnS NPs and inset of pristine ZnS NPs at 300 K.

Table 2B.6. Mössbauer spectroscopic data for $Zn_{1-x}Fe_xS$ NPs.

$Zn_{1-x}Fe_xS$	Quadrupole splitting (mm/s) (±0.04)		Isomer Shift (mm/s) (±0.04)		Fractional Area	
	A	B	A	B	A	B
X=0.012	0.85	0.52	0.35	0.32	0.24	0.69
X=0.05	0.82	0.50	0.33	0.38	0.29	0.71
X=0.10	0.83	0.52	0.35	0.36	0.31	0.76

Table 2B.7. The VSM data at room temperature for ZnS NPs doped with different amounts of Fe.

Parameter	ZnS Pristine	ZnS:Fe (1.2%)	ZnS:Fe (5.0%)	ZnS:Fe (10.0%)
Susceptibility (χ)	-0.097	6.29×10^{-7}	1.5×10^{-6}	3.6×10^{-6}
Retentivity (emu/g)	1.15×10^{-4}	5.08×10^{-4}	1.88×10^{-3}	3.56×10^{-3}
Ms (emu/g)	1.22×10^{-3}	0.01	0.03	0.07
Coercivity (G)	2211.0	437.11	660.16	318.25

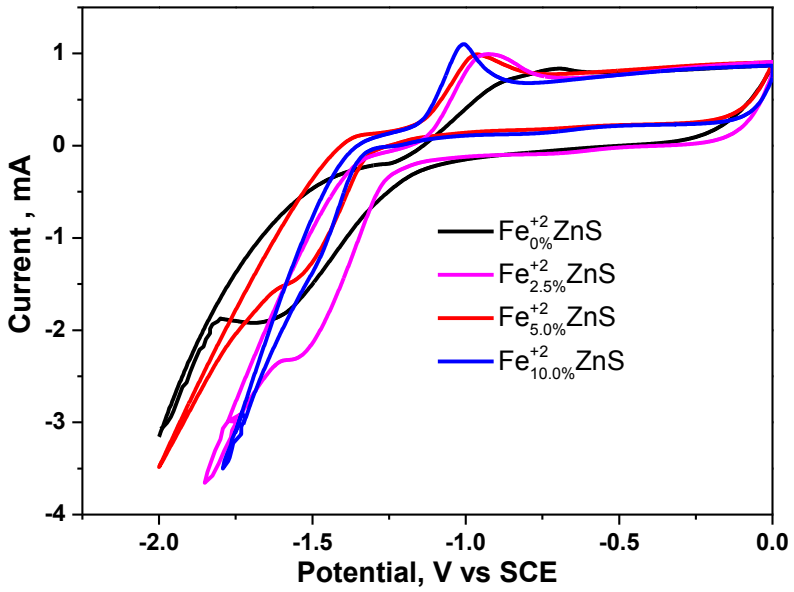

Figure 2B.21. Cyclic Voltammogram of Fe^{2+} doped and pristine ZnS NPs as a working electrode in aqueous solution (Scan rate: 25mV/Sec. RE= saturated calomel electrode (SCE), CE= platinum wire).

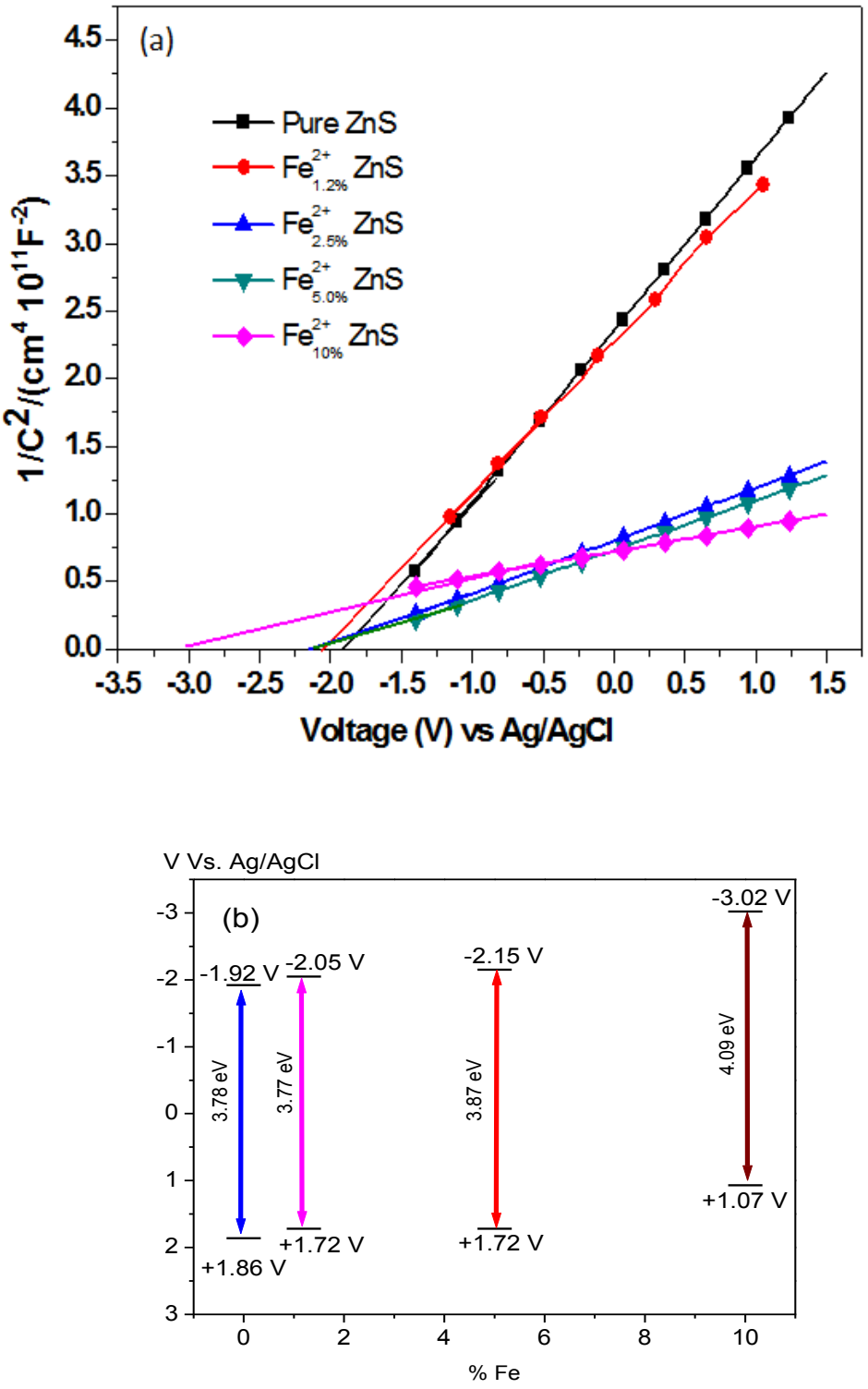

Figure 2B.22 (a) Normalized Mott-Schottky plot (b) band structure picture of ZnS NPs with different dopant level.

It can be observed that as dopant level increases there is a very small increment in the band width which can be compensated by the energy levels provided from the dopant ions. However, at 10% dopant level, there is a large increase in the band gap which shifts the light absorption in the uv region.

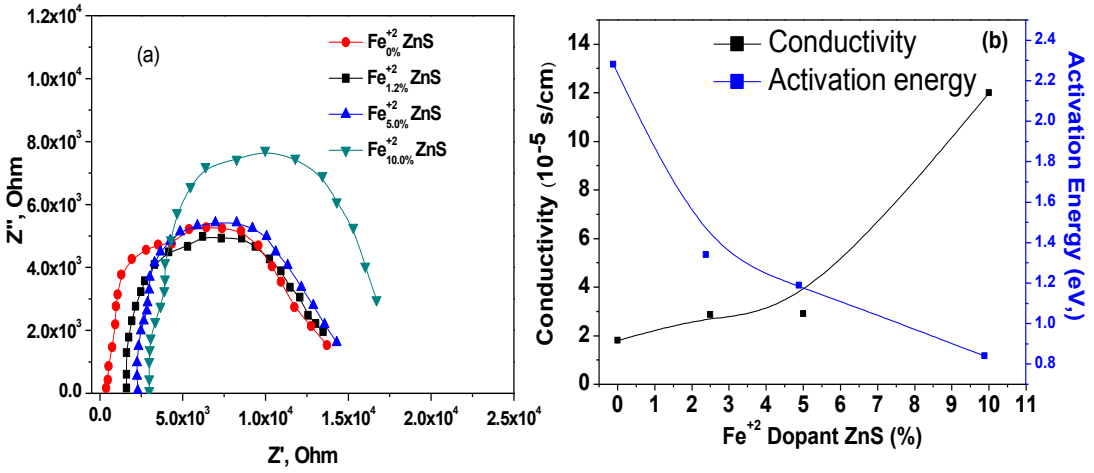

Figure 2B.23 (a) EIS Nyquist plots and (b) Activation energy diagram at 30°C for ZnS NPs with different dopant concentration. The EIS measurements were performed for different Fe doped ZnS NPs pallets placed between the two conducting aluminum pallets and measurements in dark were conducted in the frequency range 0.1 Hz to 1.2 MHz with AC amplitude of 10 mV.

Figure 2B.23 (a) presents typical electrochemical impedance spectra (EIS) as Nyquist plots, and it is observed that the diameter of the semicircle in the plot remains almost constant upto 5% and then decreases at 10%. There is gradual increase in conductance upto 10% also as shown in Figure. 2B.23(b). These may be due to trapping of the charge carriers at the impurity level or defects produced due to dopant impurities. Further, it can be observed from the Figure 2B.23(b) that the activation energy (energy requires for the charge carriers to overcome the solid-state interface layer resistance and the charge-transfer resistance on the electrode surface) [56] decreases with little rise in conductance on introduction of the dopant ions.

Proposed Mechanism of photocatalysis

When light photon falls on semiconducting ZnS NPs, the electron from VB gets excited to CB, forming exciton. The dopant ions (Fe^{3+}) present in the surrounding trap this electron and form Fe^{2+} ion leaving a hole behind in VB. During these photophysical processes, the holes present in VB oxidize Fe^{2+} to Fe^{3+} and synergistically enhance the photocatalytic activity by generating ·OH free radical from water. Thus, Fe^{2+}-Fe^{3+} redox couple continuously pumps the electrons from VB to CB and also channels them to the adsorbed dye molecules. So at any time both Fe^{2+} and Fe^{3+} can be found in the material which is confirmed from Mössbauer spectroscopy and CV analysis. It is known that doping of 3d transition metal ions can bring free charge carriers, due to the difference between the valances of 3d ion and the cation in VB [57]. Thus, by raising the amount of dopant ions (Fe^{2+}/Fe^{3+}) in the ZnS matrix, charge carrier density increases. Due to presence of excess amount of charge in the material, the dopant Fe ions, which are uniformly distributed in the material, communicate with one another and exhibit charge carrier mediated ferromagnetic interaction at room temperature in agreement with VSM analysis [58].

Table 2B.8. MS and EIS data of pristine and Fe doped ZnS NPs.

Amount of Fe as dopant in ZnS NPs. (%)	Conductivity (10^{-5} S/cm)	Activation Energy (eV, kJ/mol)	Donor density $(N_d)/cm^{-3}$
0	1.80	2.28	1.33×10^{18}
1.2	2.86	1.34	3.95×10^{18}
5.0	2.90	1.19	4.72×10^{18}
10.0	12.0	0.84	9.44×10^{18}

Table 2B.9. Electronic band structure of the photocatalyst.

% Fe as dopant in ZnS NPs	Slope from MS plot	$E_{cb} \sim E_{fb}$ vs. Ag/AgCl V	$E_{cb} \sim E_{fb}$ vs. NHE V	Band gap energy eV	E_{VB} V
0	1.27	-1.92	-1.72	3.78	+1.86
1.2	0.43	-2.05	-1.85	3.77	+1.72
5.0	0.36	-2.15	-1.95	3.87	+1.72
10.0	0.18	-3.02	-2.82	4.09	+1.07

Conclusion

ZnS NPs, pristine as well as with different amount of Fe (1.2, 5.0, and 10% by wt) were synthesized by simple wet chemical method. From this study it can be concluded that 5% Fe doped ZnS NPs show optimum photocatalytic activity due to (1) mesoporous entangled rods having rough surfaces (2) maximum surface stabilization due to charge distribution and (3) predesigned energy levels constructed below CB and above VB of the semiconducting host material. The distribution of dopant ions in Fe^{2+} and Fe^{3+} states plays an important role. Electrons from CB and defects at Fe^{3+} and Fe^{2+} sites get pumped towards the adsorbate and during this process if Fe^{2+} / Fe^{3+} are uniformly distributed, charge carrier mediated magnetic interaction between Fe^{2+} and Fe^{3+} can be observed. Both types of degradation mechanisms (direct degradation on the surface of adsorbent as well as $\cdot OH/O_2^{\cdot -}$ free radicals mediated degradation) can be activated concurrently by proper designing of the catalyst. As the amount of dopant ions increases from 0 to 10%, donor density increases, directly affecting the performance of the material. The balance among distribution, location and oxidation states of dopant ions, levels of defects, crystallinity and charge carrier density are all significant in achieving optimum performance from the material as photocatalyst.

References

[1] C.L. Torres-Martínez, R. Kho, O.I. Mian, R.K. Mehra, *J. Colloid Interface Sci.***2001**, 240, 525.

[2] D. Beydoun, R. Amal, G. Low, S. McEvoy, *J. Nanopart. Res.***1999**, 1, 439.

[3] K.N. Ferreira, T.M. Iverson, K. Maghlaoui, J. Barber, S. Iwata, *Science* **2004**, 303, 1831.

[4] S. Fukuzumi, K. Ohkubo, T. Suenobu, *Acc. Chem. Res.* **2014**, 47, 1455.

[5] M. Grätzel, *Cattech*. **1999**, *3*, 4.

[6] A. Mills, S.L. Hunte, *J. Photochem. Photobiol. A- Chem.* **1997**, 108, 1.

[7] A. Kudo, *Pure Appl. Chem.* **2007**,79, 1917.

[8] A. Kudo, M. Sekizawa, *Chem. Commun.* **2000**, 1371.

[9] Y. Wada, H. Yin, T. Kitamura, S. Yanagida, *Chem. Commun.* **1998**, 24, 2683.

[10] A.J. Nozik, M.C. Beard, J.M. Luther, M. Law, R.J. Ellinggson, J.C. Johnson, *Chem. Rev.* **2010**, 110, 6873.

[11] I. J. Kramer, E. H. Sergent, *ACS Nano* **2011**, 5, 8506.

[12] F. Hetsch, N. Zhao, S.V. Kershaw, A.L. Rogach, *Mater. Today* **2013**, 16, 312.

[13] R. Hanson, L.P. Kouwenhoven, J.R. Petta, S. Tarucha, L.M.K. Vandersypen, *Rev. Mod. Phys.* **2007**, 79, 1217.

[14] A.S. Dzurak, J.R. Petta, E.L. Hu, L.C. Bassett, D.D. Awschalom, *Science* **2013**, 339, 1174.

[15] S.-C. Ke, T.-C. Wang, M.–S. Wong, N.O. Gopal, *J. Phys. Chem. B* **2006**, 110, 11628.

[16] E.A. Weiss, *Acc. Chem. Res.***2013**, 46, 2607.

[17] D. Zhang, G. Li, H. Li, Y. Lu, *Chem. Asian J.***2013**, 8, 26.

[18] W. Xu, P. K. Jain, B.J. Beberwyck, A. P. Alivisatos, *J. Am. Chem. Soc.* **2012**, 134, 3946.

[19] H. Platz, P.W. Schenk, *Angew. Chem. Int. Ed.***1936**, 49, 822.

[20] A. Henglein, *Pure Appl. Chem.***1984**, 56, 1215.

[21] N. Dixit, N. Anasane, M. Chavda, D. Bodas, H.P. Soni, *Cryst. Res. Technol.***2012**, 47, 1105.

[22] The spectrum from HPMV light and its comparison with natural light is available at http://micro.magnet.fsu.edu/primer/lightandcolor/lightsourcesintro.html.

[23] R. Chauhan, A. Kumar, R. P. Chaudhary, *J. Lumin.* **2014**, 145, 6.

[24] R. Jenkins, R. L. Snyder in *Introduction to X-ray powder diffractometry*,J. Wiley &Sons, NewYork, **1996**.

[25] Z. Jindal, N.K. Verma, *J. Mater. Sci* **2008**, 43, 6539.

[26] X. Wang, Y. Du, H. Liu, *Preparation, Carbohydr. Polym.* **2004**, 56, 21.

[27] K.S.W. Sing, D.H. Everett, R.A.W. Haul, L. Moscou, R.A. Pierotti, J. Rouquerol, T. Siemieniewska, *Pure Appl. Chem.* **1985**, 57, 603.

[28] J. Yu, L. Zhang, B. Cheng, Y. Su, *J. Phys. Chem.* C **2007**, 111, 10582.

[29] D.F. Zhang, L.D. Sun, J.L. Yin, C.H. Yan, R.M. Wang, *J. Phys. Chem. C* **2005**, 109, 8786.

[30] J.M. Berg, A. Romoser, N. Banerjee, R. Zebda, C.M. Sayes, *Nanotoxicology* **2009**, 3, 276.

[31] R. Rossetti, R. Hull, J. M. Gibson, L.E. Brus, *J. Chem. Phys.* **1985**, 82, 552.

[32] J. I. Pankov, *Optical Processes in Semiconductors*, Prentice-Hall, New Jersey, **1971**.

[33] J. Yan, G. Wu, N. Guan, L. Li, Z. Li, X. Cao, *Phys. Chem. Chem. Phys.* **2013**, *15*, 10978.

[34] X. Chen, X. Wang, Y. Hou, J. Huang, L. Wu, X. Fu, *J. Catal.* **2008**, 255, 59.

[35] N. Dixit, H.P. Soni, *Superlattices Microstruct.* **2014**, 65, 344.

[36] M. Sharma, S. Kumar, O.P. Pandey, *J. Nanopart. Res.* **2010**,12, 2655.

[37] M. Sharma, T. Jain, S. Singh, O.P. Pandey, *Solar Energy* **2012**, 86, 626.

[38] D. Wu, B. Xiao, N. Liu, Y. Xiao, K. Jiang, *Mater. Sci. Eng. B* **2010**, 175, 195-200.

[39] H.R. Pouretedal, A. Norozi, M.H. Keshavarz, A. Semnani, J. *Hazard. Mater.* **2009**, 162, 674.

[40] T. Arthi, P. Narahari, G. Madras, *J. Hazard. Mater.* **2007**, 149, 725.

[41] H. Fu, C. Pan, W. Yao, Y. Zhu, *J. Phys. Chem. B* **2005**, 109, 22432.

[42] C. Chen, W. Zhao, J. Li, J. Zhao, *Environ. Sci. Technol.* **2002**, 36, 3604.

[43] J.C. Colmenares, R. Luque, *Chem.Soc. Rev.* **2014**, 43, 765.

[44] Q. Xiao, Z.C. Si, J. Zhang, C. Xiao, X.K. Tan, *J. Hazard. Mater.* **2008**, 150, 62.

[45] K. Ishibashi, A. Fujishima, T. Watanabe, K. Hashimoto, *Electrochem. Commun.***2000**, 2, 207.

[46] V.G. Blade in *Mossbauer Effect and its applications*, Tata McGraw Hill, New Delhi, India, **1973**.

[47] D.R.S. Somayajulu, M. Chawda, N. Patel, M. Sarkar, K.C. Sebastian, K. Venugopalan, A. Gupta, *Appl. Phys. Lett.***2005**, 87, 242508.

[48] F.–R.F. Fan, P. Leempoel, A.J. Bard, *J. Electrochem. Soc.* **1983,** 130, 1866.

[49] A. W. Bott, *Current Separations* **1998**, 17, 87.

[50] G. Wang, Q. Wang, W. Lu, J. Li, *J. Phys. Chem. B* **2006**, 110, 22029.

[51] W.–D. Zhang, L.–C. Jiang, J.–S. Ye, *J. Phys. Chem. C* **2009**, 113, 16247.

[52] H. Kisch, *Angew. Chem. Int. Ed.* **2013**, 52, 812.

[53] S. Zhang, J. Li, M. Zeng, J. Li, J. Xu, X. Wang, *Chem. Eur. J.* **2014**, 20, 9805.

[54] M. E. Orazem, B. Tribollet in *Electrochemical impedance spectroscopy*, J. Wiley &Sons, New Jersey,**2008**, pp. 229.

[55] K. Gelderman, L. Lee, S. W. Donne, *J. Chem. Educ.* **2007**, 84, 685.

[56] M. Petrowsky, R. Frech, *J. Phys. Chem. B* **2009,** 113, 5996.

[57] N. Agrawal, M. Sarkar, M. Chawda, V. Ganesan, *Mater.Chem. Phys.* **2013**, 143, 330 .

[58] S. Bhattacharya, D. Chakravorty, *Chem. Phys. Lett.* **2007**, 444, 319.